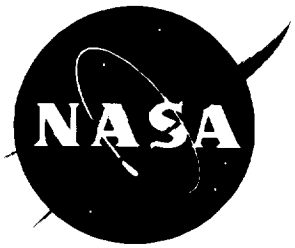

NASA Contractor Report 4626

Micromechanics of Fatigue in Woven and Stitched Composites

B. N. Cox, W. C. Carter, M. S. Dadkhah, and W. L. Morris
Rockwell International Science Center • Thousand Oaks, California

National Aeronautics and Space Administration
Langley Research Center • Hampton, Virginia 23681-0001

Prepared for Langley Research Center
under Contract NAS1-18840

September 1994

Table of Contents

List of Figures

List of Figures (Cont'd)

List of Figures (Cont'd)

List of Tables

Personnel

Brian Cox (program manager)

Craig Carter

Mahyar Dadkhah

Jonathan Flintoff

Fred Morris

Acknowledgments

The authors are grateful to Dr. Norman Fleck for significant contributions to formulating the Binary Model.

Inspiration was drawn throughout this research from the activities of the textiles working group in the Advanced Composites Technology Program at NASA Langley. The authors are especially pleased to recognize the guiding influence of Drs. C.E. Harris and C.C. Poe in that program.

Summary

The goals of this research program were to

(i) determine how microstructural factors, especially the architecture of reinforcing fibers, control stiffness, strength, and fatigue life in 3D woven composites;

(ii) identify mechanisms of failure;

(iii) model composite stiffness;

(iv) model notched and unnotched strength; and

(v) model fatigue life.

We have examined a total of eleven different angle and orthogonal interlock woven composites. Extensive testing has revealed that these 3D woven composites possess an extraordinary combination of strength, damage tolerance, and notch insensitivity in compression and tension and in monotonic and cyclic loading. In many important regards, 3D woven composites far outstrip conventional 2D laminates or stitched laminates. Detailed microscopic analysis of damage has led to a comprehensive picture of the essential mechanisms of failure and how they are related to the reinforcement geometry. The critical characteristics of the weave architecture that promote favorable properties have been identified. Key parameters are tow size and the distributions in space and strength of geometrical flaws. The geometrical flaws should be regarded as controllable characteristics of the weave in design and manufacture.

In addressing our goals, the simplest possible models of properties were always sought, in a blend of old and new modeling concepts. Nevertheless, certain properties, especially regarding damage tolerance, ultimate failure, and the detailed effects of weave architecture, require computationally intensive stochastic modeling. We have developed a new model, the "Binary Model", to carry out such tasks in the most efficient manner and with faithful representation of crucial mechanisms.

This is the final report for contract NAS1-18840. It covers all work from April 1989 up to the conclusion of the program in January 1993.

1. Introduction

Recent advances in resin transfer molding have made possible the manufacture of high volume fraction composites from a great variety of dry fiber preforms. The most interesting of these have three-dimensional (3D) reinforcement, in which the fibers alone carry loads in each of three linearly independent directions. Dry 3D preforms can be manufactured by weaving, braiding, stitching, or knitting [e.g., 1-5].

3D polymer composites have been pursued in the aerospace industry largely in reaction to the vulnerability of conventional laminates to delamination under impact and subsequent failure by buckling under in-plane compression. In this regard, they have been successful [3,4,6,7]. It is now becoming clear that they have outstripped this goal by also exhibiting extraordinary properties under in-plane loading in their pristine condition. Following their 3D carbon-carbon composite ancestors [e.g., 8], certain 3D polymer composites offer large strains to failure[1] , suggesting notch insensitivity and damage tolerance far beyond those of 2D laminates.

In early work under this contract [9], high strains to failure of 3D woven interlock composites under uniaxial compression were linked to broad distributions of geometrical flaws in strength and space. The geometrical flaws comprise both misalignment of nominally straight load bearing tows and certain topological features of the weave architecture. Geometrical flaws lower the critical value of the local stress for kink band formation, which was determined to be the primary mechanism for failure.

In tension and bending, damage tolerance is again far in excess of that typical of conventional 2D laminates. Consideration of the mechanics of the observed failure events leads to general remarks about the origins of such behavior. Once again, geometrical flaws appear to have a vital role.

The mechanisms of damage observed in fatigue are closely related to those seen under monotonic loading. Ultimate failure again tends to be associated with broadly distributed damage and high energy absorption.

[1] Throughout this report, strain to failure will refer to the strain at which any specimen ceased to bear load when tested under stroke control. The strain failure so defined is always equal to or greater than the strain to peak load; it is often much greater.

All our experimental observations form the basis for models for design and reliability in monotonic and cyclic loading. The first generation of these models is also reported here.

2. Materials

The subject materials were various 3D interlock weaves impregnated and consolidated with epoxy resin. Eleven different composites were studied in all. The weaver's specifications for the reinforcement in each case are listed in Table 1. As also indicated in Table 1, the eleven materials can be conveniently divided into two groups according to the degree of fiber compaction achieved during processing.

Table 1

Weaver's Specifications for Reinforcement

Preform Label	Architecture	Warp Weaver Material	Tow Denier[a] Stuffers	Fillers	Weavers	Number of Layers of Stuffers	Ends per cm (inch)[b]	Picks per cm (inch)[c]
(a) Lightly Compacted (Resin: Dow Tactix 138 with H41 hardener[†])								
l-L-1	Layer-to-Layer	AS4	13.8k	13.8k	5.9k	4	5.1 (13)	4.4 (11.3)
l-L-2	Angle Interlock	S-2 glass	13.8k	13.8k	5.95k	4	5.1 (13)	5.9 (15)
l-T-1	Through-the-Thickness	AS4	13.8k	13.8k	5.9k	4	4.7 (12)	5.0 (12.7)
l-T-2	Angle Interlock	S-2 glass	13.8k	13.8k	5.95k	4	5.1 (13)	5.0 (12.7)
l- O	Orthogonal Interlock	AS4	13.8k	13.8k	5.9k	4	4.7 (12)	5.1 (13)
(b) Heavily Compacted (Resin: Shell RSL-1895 with EPON CURING AGENT® W*)								
h-L-1	Layer-to-Layer	AS4	15.8k	7.9k	(3.94k,0.66k)[d]	4	5.5 (14)	5.1 (13)
h-L-2	Angle Interlock	AS4	7.9k	3.94k	(1.97k,0.66k)[d]	6	7.1 (18)	7.9 (20)
h-T-1	Through-the-Thickness	AS4	15.8k	7.9k	3.94k	4	5.5 (14)	5.1 (13)
h-T-2	Angle Interlock	AS4	7.9k	3.94k	1.97k	6	7.1 (18)	7.9 (20)
h-O-1	Orthogonal Interlock	AS4	15.8k	7.9k	3.94k	4	5.5 (14)	5.1 (13)
h-O-2	Orthogonal Interlock	AS4	7.9k	3.94k	1.97k	6	7.1 (18)	7.9 (20)

[a] For AS4 fibers, a tow denier of 13.8k corresponds to a filament count (fibers per tow) of 21,000, 15.8k to a count of 24,000, 7.9k to 12,000, ...0.66k to 1000.
[b] number of columns of stuffers per cm (inch) in weft direction.
[c] number of columns of fillers per cm (inch) in warp direction.
[d] The first figure refers to warp weavers, the second to surface warp weavers.

[†] Dow Chemical Co., Freeport, Texas
[*] Shell Oil Co., Anaheim, California

All fiber preforms were supplied by Textile Technologies, Inc.[†] The "lightly compacted composites" were processed by the authors and their colleagues by methods described fully in Appendix A, using Dow Tactix 138 resin with H41 hardener. The dry preforms in this group were relatively loosely woven and minimal compaction pressure was applied to them in the through-thickness direction during consolidation. The resulting composites possess relatively low

[†] Textile Technologies, Inc., Hatboro, Pennsylvania.

total fiber volume fractions. The "heavily compacted composites" were processed by Boeing* using Shell 1895 resin with a cure cycle of 30 min. at 149°C and 90 min. at 177°C, followed by a further 2 hr. post cure at 177°C [10]. The dry preforms in this group were relatively tightly woven. Substantial through-thickness pressure (1.5 MPa) during consolidation produced some further compaction and ensured the attainment of predetermined thicknesses for each composite. The resulting volume fractions were relatively high. Because of the higher volume fractions and the lower weight per unit area of the dry fiber preforms, the heavily compacted composites were only half as thick as the lightly compacted ones (Table 2).

Table 2

Fiber Volume Fractions

Composite	Specimen Thickness (cm)[a]	Nominal Volume Fractions			Total Fiber Volume Fraction[e]	Fraction by Volume of All Fibers Lying in:[f]		
						Stuffers	Fillers	Warp Weavers
		V_s[b]	V_f[c]	V_w[d]	V	f_s	f_f	f_w
l-L-1	1.26	0.14	0.15	0.07	0.35 ± 0.03	0.385	0.418	0.197
l-L-2	1.24	0.14	0.20	0.05	0.370 ± 0.005[g] 0.066 ± 0.004[h]	0.347	0.502	0.151
l-T-1	1.02	0.16	0.21	0.05	0.466 ± 0.003	0.381	0.504	0.115
l-T-2	0.97	0.18	0.22	0.04	0.408 ± 0.020[g] 0.044 ± 0.004[h]	0.406	0.497	0.097
l-O	0.88	0.18	0.25	0.04	0.483 ± 0.010	0.387	0.524	0.090
h-L-1	0.561	0.38	0.22	0.05	0.620 ± 0.008	0.587	0.340	0.073
h-L-2	0.625	0.33	0.21	0.025	0.557 ± 0.015	0.580	0.375	0.045
h-T-1	0.573	0.37	0.22	0.065	0.613 ± 0.003	0.571	0.331	0.098
h-T-2	0.577	0.36	0.23	0.035	0.592 ± 0.014	0.571	0.369	0.059
h-O-1	0.579	0.37	0.22	0.045	0.619 ± 0.008	0.586	0.340	0.073
h-O-2	0.587	0.35	0.23	0.065	0.593 ± 0.014	0.545	0.353	0.102

[a] in direction normal to warp and weft directions.
[b] V_s ≡ volume fraction of stuffer (straight warp) tows.
[c] V_f ≡ volume fraction of filler (weft) tows.
[d] V_w ≡ volume fraction of warp weaver (3D warp) tows.
[e] measured by acid digestion.
[f] determined from weaver's specifications.
[g] graphite fibers.
[h] glass fibers.

The angle and orthogonal interlock architectures are shown schematically in Fig. 1. The stuffers (straight warp) and fillers (straight weft) form a 0°/90° array resembling a coarse laminate, but with individual tows remaining distinct within each lamina. Figure 1 shows projections on planes normal to the filler direction of architectures representative of those in Table 1. Progressing down the filler direction, planes containing a full complement of stuffers generally alternate with planes containing two warp weavers in the case of angle interlock weaves and one warp weaver in the case of orthogonal interlock weaves. The phases of the warp weavers encountered in successive planes are varied to minimize short range order. In the thicker orthogonal interlock

* Boeing Aircraft Co., Seattle, Washington.

composites, planes containing a warp weaver are alternated with two layers of stuffers to limit the volume fraction of the warp weavers to the desired range.

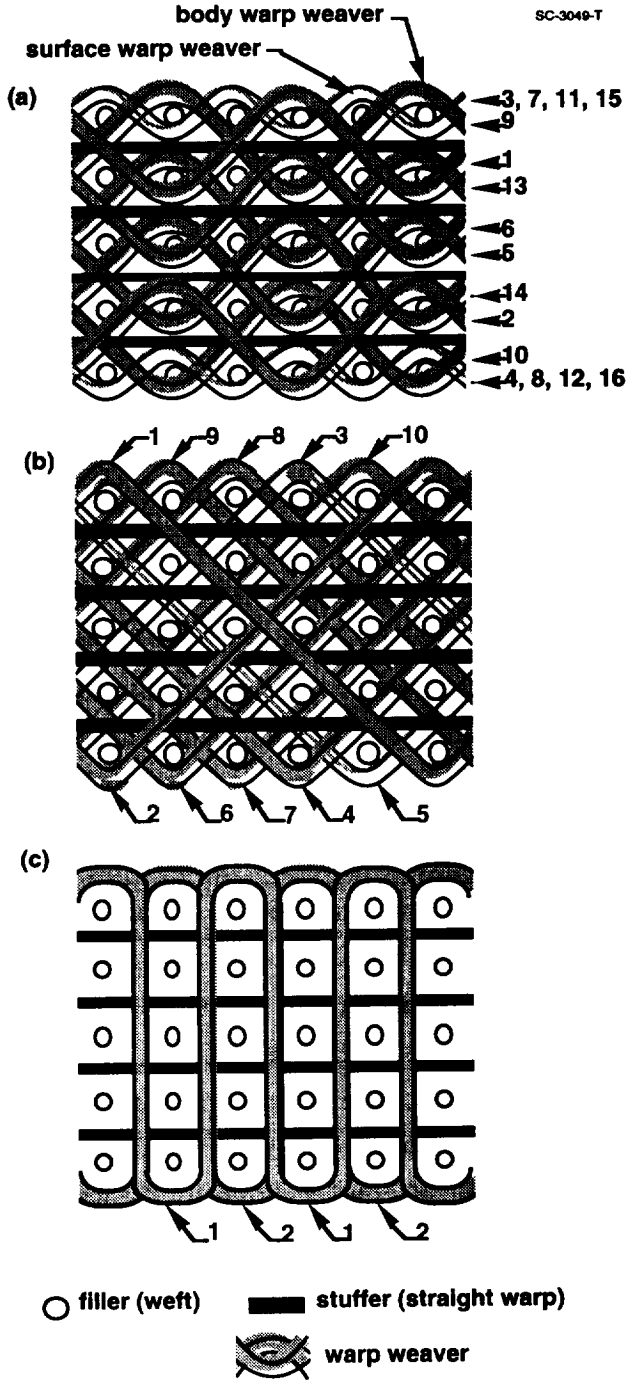

Fig. 1 Schematics of (a) layer-to-layer angle interlock (b) through-the-thickness angle interlock, and (c) orthogonal interlock weaves. Numbers indicate typical sequences in which warp weavers are encountered on progressing down the filler direction.

Table 2 summarizes fiber volume fraction data for all the composites. The nominal volume fractions for each kind of tow are deduced from the weaver's specifications of Table 1 and the measured composite thickness of Table 2. Following the ideal geometry of Fig. 1, the stuffers and fillers are assumed straight in these estimates, while the warp weavers are assigned a "take up factor", which is the ratio of the measured length of representative warp weavers drawn from a woven preform to the length of preform from which they have been drawn. The take up factor is typically ~ 1.2 for layer-to-layer angle interlock weaves, ~ 1.3 for through-the-thickness angle interlock weaves, and between 3 and 5 for orthogonal interlock weaves. Since the warp weavers contribute relatively lightly to the overall fiber content, the precise value of the take up factor has a small influence on in-plane property estimates. In practice, some departure from these nominal volume fractions is to be expected, because variations may occur in the tightness of the fabric and sizing on fibers influences the specified tow denier. Therefore, the total volume fraction, V, constituted by all fibers was measured for each composite by weighing the fibers in a known volume after acid digestion of the resin (following the procedure in ASTM Standard D3171). The value of V differs from the sum of the nominal volume fractions by as much as 10%. Regarding V as the more accurate and reliable figure, the volume fractions of fibers in the different kinds of tows can be deduced from it with reasonable confidence by assuming that the proportions of all fibers in each kind of tow remain as deduced from the weaver's specifications; i.e., in the ratios V_s:V_f:V_w. The variables f_s, f_f, and f_w in Table 2 denote the fractions by volume of all fibers lying in stuffers, fillers, and weavers, respectively, so determined.

Both the lightly and heavily compacted composites deviate substantially from the nominal or ideal pattern of straight stuffers and fillers and approximately sawtooth, square wave, or sinusoidal warp weavers. One of the main aberrations in both groups is the distortion of the fillers and stuffers near sites where warp weavers wrap around fillers, as in the schematic of Fig. 2. In occurrences of this configuration at the specimen surface, the warp weaver is sometimes separated from the surface by a pocket of resin, implying that the distortion must have arisen during weaving as a result of tension in the warp weaver. In other occurrences, the warp weaver is pressed against the surface, implying that the distortion may be the result of through-thickness compaction during consolidation. In the lightly compacted composites, instances of the distortion of Fig. 2 tend to appear randomly throughout the structure, while in the heavily compacted composites, they tend to occur systematically, often at every warp weaver extremum. The magnitude of the distortion varies significantly from one weave type to another.

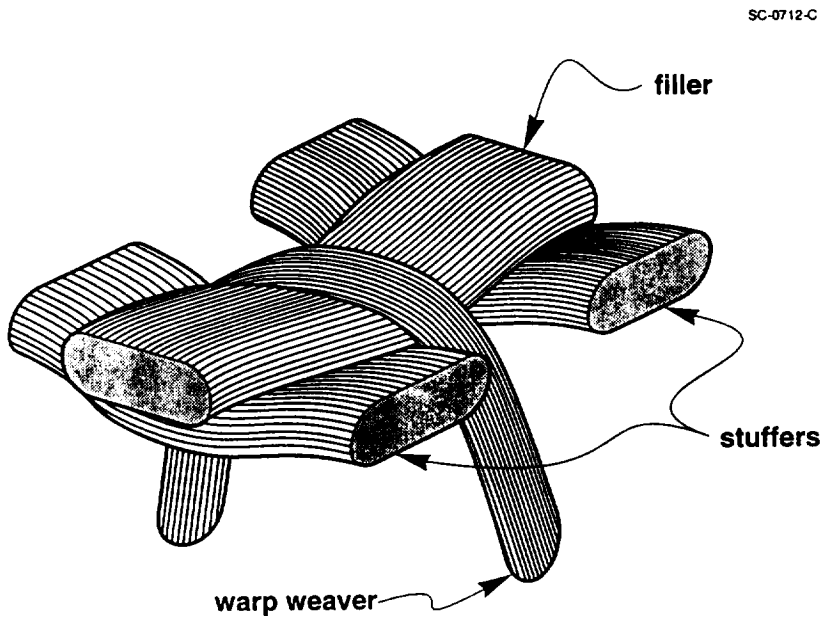

Fig. 2 Schematic of the deformation of a stuffer and filler near an extremum of a warp weaver.

In the lightly compacted composites, other random distortions of stuffers and fillers are also found. In the heavily compacted materials, the stuffers are relatively straight away from warp weaver extrema. To some extent, this difference is attributable to the difference in compaction pressure and to some extent to the fact that the fiber preforms used for the lightly compacted specimens were significantly more irregular as received from the weaver than those used in the heavily compacted composites. On the other hand, the fillers in heavily compacted materials are generally very heavily distorted (Fig. 3). This is perhaps attributable to the fillers being much lighter than the stuffers in the heavily compacted materials and to the fact that fillers are more directly affected by the distortion of Fig. 2.

Another significant distortion is crimping of warp weavers, as illustrated in the micrograph of Fig. 4. This distortion is generally much more severe in the heavily compacted composites. It is obviously the result of through-thickness compaction during consolidation.

Aberrations from ideal geometry are very important in determining composite properties, especially strength, strain to failure, and fatigue life.

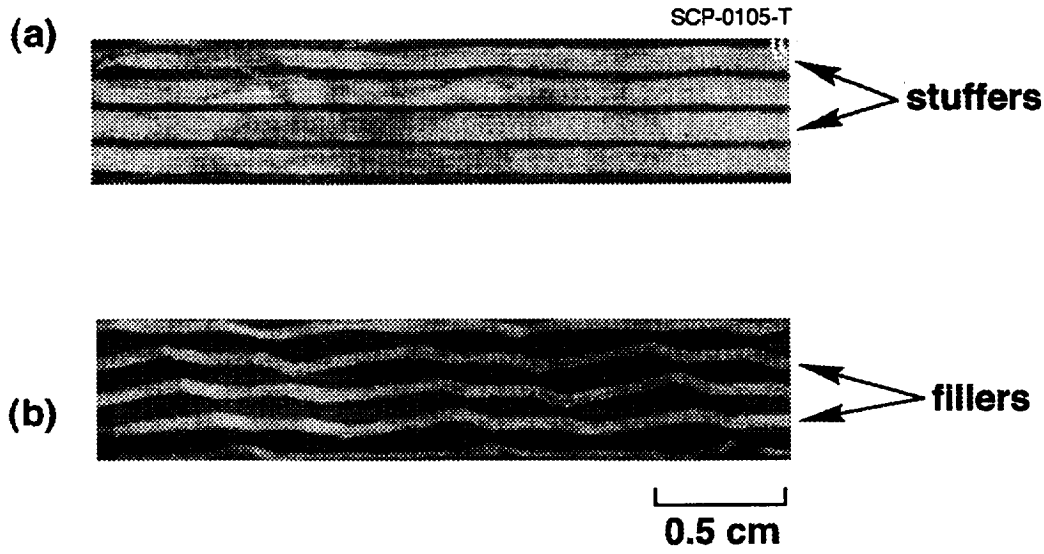

Fig. 3 Typical distortions of (a) stuffers and (b) fillers in the heavily compacted composite *h*-L-1.

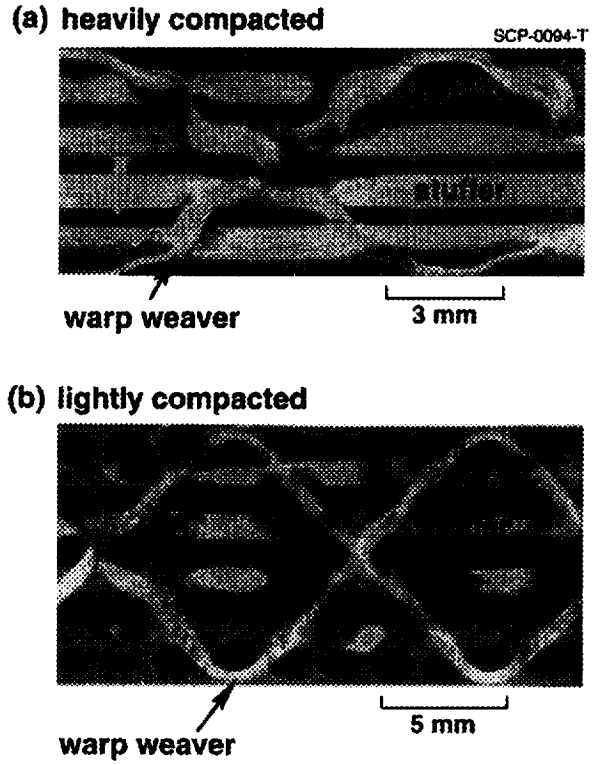

Fig. 4 Distortion of warp weavers in angle interlock woven composites that are (a) heavily compacted and (b) lightly compacted.

3. Monotonic Loading

3.1 Experiments and Observations

Because our ultimate goal has been to formulate mechanism-based design and reliability models, the experiments reported here were not planned to provide comprehensive engineering data for all the composites studied. Emphasis lay instead on associating typical macroscopic properties with failure mechanisms and identifying microstructural aspects of the composites upon which the failure mechanisms depend. Tabulated data usually refer to a single test for each composite type in Table 1, the exceptions being those results for which experimental scatter is indicated.

This section reports tests conducted under monotonic loading. Fatigue tests are reported in Section 4. Tests comprised uniaxial tension and compression using dogbone specimens, compression of short cuboidal specimens between flat platens, and four-point and three-point bending of long rectangular bars. The thickness of all specimens was that of the original composite panel, with all machining cuts made normal to the original surfaces. Satisfactorily smooth and damage-free cut surfaces were obtained using a water jet.

Dogbone specimens for the lightly compacted composites had straight sided gauge sections approximately 2.4 cm long and 1.1 cm wide (Fig. 5a). For the heavily compacted composites, some experimentation with specimen shape was required to induce failures in the gauge section. The final specimen shape, which was almost universally successful in this regard, was that of Fig. 5b. Short cuboidal specimens were approximately 2.1 cm long and 1 cm wide. Bending bars were approximately 12.5 cm long and 1 cm wide, with moment arms of 5.7 cm and 2.9 cm for three-point and four-point bending respectively.

In all compression and tension tests, the long axis of the specimen and therefore the load axis were aligned with the stuffers.† In bending tests, bending was applied about an axis parallel to the fillers.

† Tests with loading along the filler direction will be reported under our new contract NAS1-19243. All aspects of modeling for this load orientation are qualitatively identical to the modeling reported here.

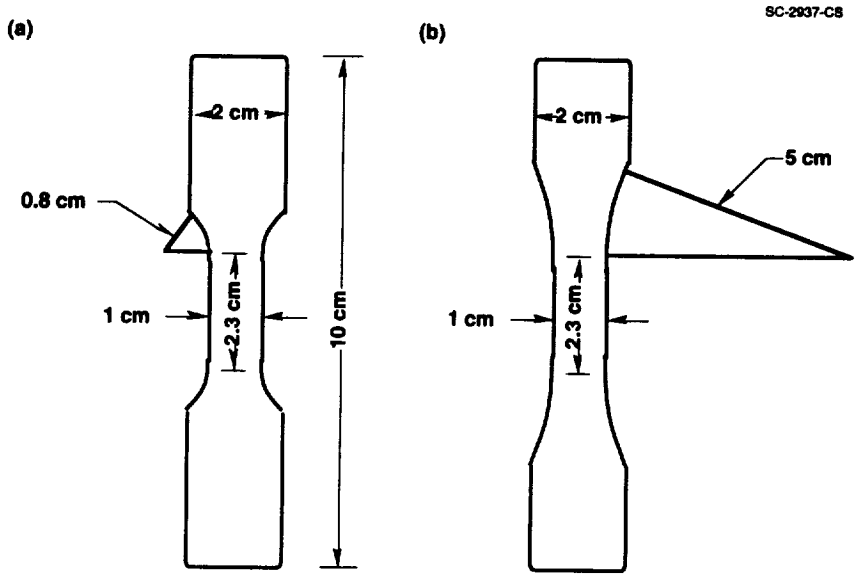

Fig. 5 Dogbone specimen dimensions for tests of (a) lightly and (b) heavily compacted composites.

3.1.1 Compression Tests

All tests were conducted under displacement control. For compression tests, the controlled displacement was the stroke of the test apparatus. Stress-strain curves are presented in Fig. 6.

Test data for the first four lightly compacted composites of Table 1 are summarized in Tables 3 and 4. These particular materials have high strains to failure under compression, in contrast to conventional 2D laminates or stitched laminates, which fail in a brittle manner. The ductility is due to the action of geometrical flaws, which consist of either the misalignment of nominally straight tows or certain topological features of the reinforcement architecture. Details of this crucial idea appear in [1] and below.

Test data for compression tests of heavily compacted composites are summarized in Table 5. For both dogbone and cuboidal specimens, substantial nonlinearity sets in at less than half the peak load or at strains ~ 0.5%. The figure quoted in Table 5 for the modulus is that for the approximately linear regime at low stresses. In the dogbone tests, softening sometimes reflected Euler buckling of the entire specimen. While buckling was rarely observed in tests of lightly compacted composites, it is much harder to suppress in the heavily compacted composites because they are only half as thick. For the cuboidal specimens, initial nonlinearity can be caused by the constraint of the specimen ends and Poisson's effect, which combine to cause the lateral surfaces

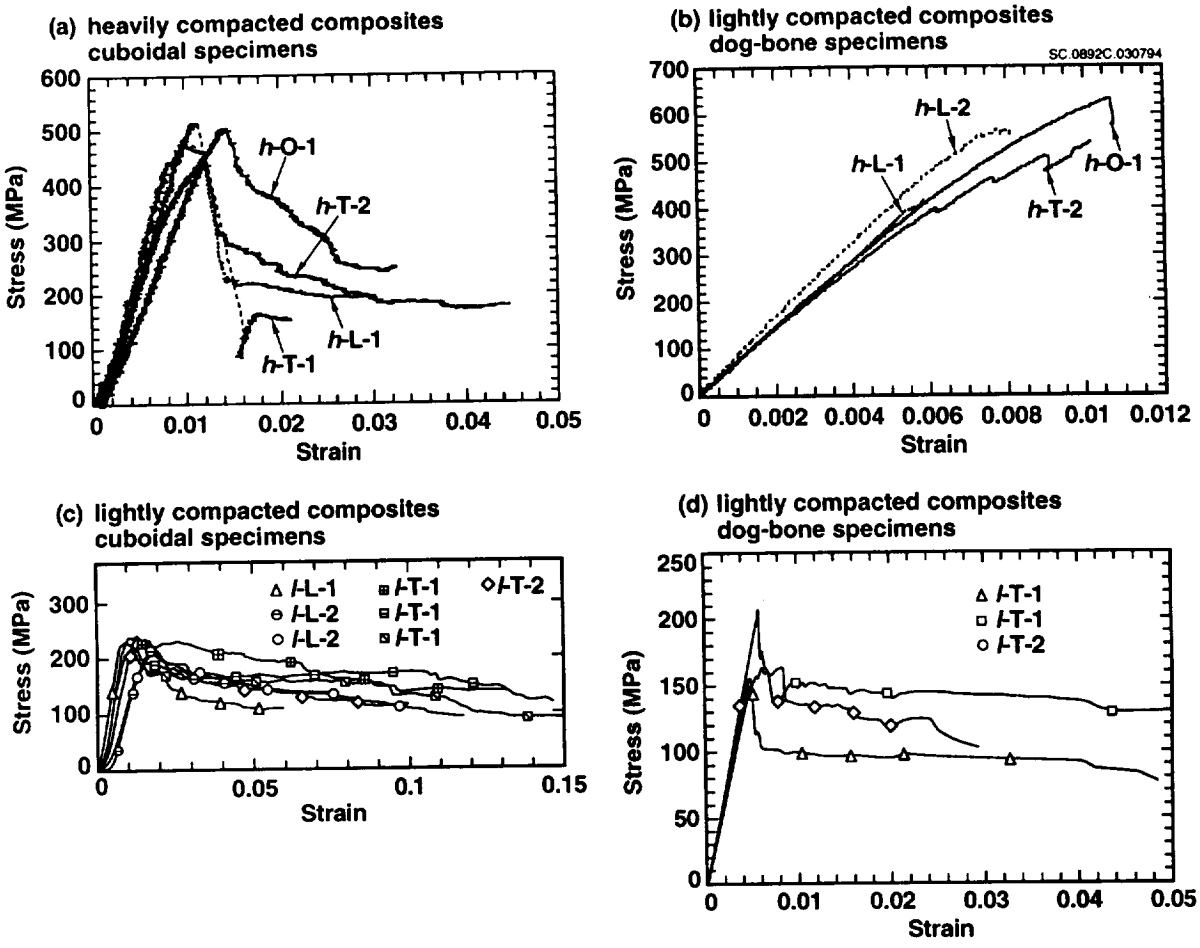

Fig. 6 Stress-strain curves for monotonic uniaxial compression in the stuffer direction.

Table 3

Data for Cuboidal Test Specimen—Lightly Compacted Composites

	Specimen label	V_s[a]	Maximum compressive stress (MPa)	Modulus (GPa)	ε_m[b]	$\varepsilon_{1/2}$[c]
Woven composites	*l*-L-1	0.28	230	35	0.0095	0.06
	l-L-2(I)	0.23	215	23	0.012	0.09
	l-L-2(II)	0.20	205	20	0.012	0.12
	l-T-1(I)	0.33	240	38	0.012	0.16
	l-T-1(II)	0.27	205	28	0.012	0.15
	l-T-1(III)	0.25	200	31	0.011	0.16
	l-L-2	0.27	240	27	0.010	0.1
Tactix 138 epoxy	e-1		105	2.9	0.079	—[d]
	e-2		115	3.06	0.080	

[a]Volume fraction of aligned fibers, including straight surface warp weavers.
[b]Compressive strain at maximum load.
[c]Compressive strain when post-peak load has fallen to half the maximum.
[d]Both tests of epoxy finished with load still exceeding half maximum.

Table 4

Data for Dog-bone Test Specimens—Lightly Compacted Composites

Specimen label	Controlled parameter	Maximum compression stress (MPa)	Modulus (GPa)	ε_m[a]	$\varepsilon_{1/2}$[b]	Method of strain measurement[c]
l-L-1(I)	strain	210	41.5	0.005		cg
l-L-1(II)	load	210	28			si
l-L-2(I)	load	140	25	0.006		cg
l-L-2(II)	strain	155	35	0.005	0.05	cg
l-L-2(III)	strain	160				
l-T-1(I)	strain	165	32.5	0.005	0.14	cg
l-T-1(II)	load	150				cg
l-T-2(I)	strain	205	35.5	0.006	0.03	cg
l-T-2(II)	strain	195	38.5	0.005	0.04	si

[a]Compressive strain at maximum load.
[b]Compressive strain when post-peak load has fallen to half of maximum.
[c]"cg" indicates a clip gauge, "si" steroimaging; in both cases, using a 1.2 cm gauge length.

Table 5

Compression Tests of Heavily Compacted Specimens

Preform Label	Maximum Compressive Stress (MPa)	Modulus (GPa)	ε_m	$\varepsilon^a_{1/2}$
Dogbone Specimens				
h-L-1	670	88	0.008	--
h-L-2	695	81	0.009	--
h-T-1	570	83	0.0078	--
h-T-2	540	72	0.0102	--
h-O-1	635	72	0.0107	--
h-O-2[b]	555 ± 15	70 ± 5	0.008	--
Cuboidal Specimens				
h-L-1	470	61	0.0108	0.0143
h-L-2[c]	--	--	--	--
h-T-1	515	52	0.0112	0.0146
h-T-2	440	42	0.0125	0.025
h-O-1	505	52	0.0142	0.0285
h-O-2[c]	--	--	--	--

[a] Strain at which the load falls to half the peak load.
[b] Two tests, both of which were terminated by Euler buckling.
[c] Not tested.

to barrel outwards, reducing stiffness because of the concomitant curvature of stuffers. Nonlinearity at strains much above 0.5% is also caused by microcracking.

The strengths of the heavily compacted specimens in compression are two to three times those reported for lightly compacted specimens (Tables 3-5). Part of the increase is attributable to the higher fiber volume fractions achieved in heavy compaction; but other factors are also significant, as discussed below.

On the other hand, the strains to failure of the heavily compacted specimens are substantially lower than those of the lightly compacted materials. The dogbone tests of heavily compacted materials reveal essentially brittle behavior, with negligible loads recorded at strains above that of the peak load. However, the apparent brittleness may have been exaggerated by

failure of the test apparatus to maintain stable stroke control after specimen buckling. The cuboidal specimens carried significant loads at strains up to ~ 3%, which far exceed the failure strains of conventional or stitched 2D laminates, but remain much lower than those recorded for the lightly compacted composites.

In contrast to lightly compacted materials, the heavily compacted materials are prone to delamination failure. While partial delaminations were previously observed in dogbone tests of the lightly compacted materials, the associated opening displacements were smaller and they were not the mechanism of ultimate failure. Ultimate failure of the lightly compacted materials was always the result of kink band formation in individual stuffers and usually occurred at much higher strains than delaminations. Figure 7a shows typical damage at high strain (~ 15%) following widespread kinking in a cuboidal specimen of the lightly compacted composite *l*-T-1. In dog-bone tests of the heavily compacted composites, ultimate failure often occurred so quickly after delamination that it was difficult to separate the two events. In such cases, the delamination itself remained one of the primary manifestations of damage. Figure 7b shows a failed cuboidal specimen of the heavily compacted composite *h*-L-1, where damage consists essentially of brooming of stuffers at one end of the specimen, with concomitant lateral displacements accommodated down the specimen by delaminations. In this particular example, it is not evident that kink bands ever formed. In most other tests where extensive delamination occurred, however, kink bands appeared to be triggered by delaminations and contributed significantly to failure.

Delamination and other factors influencing strain to failure will be discussed further in Section 3.2.

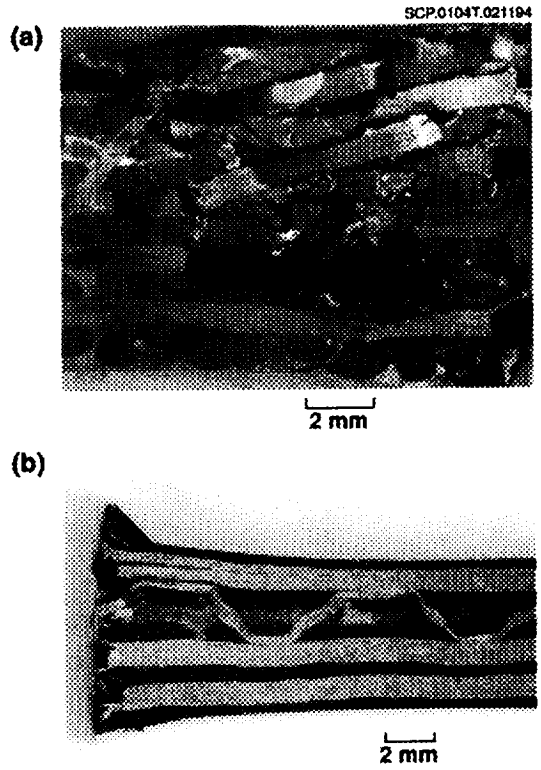

Fig. 7 Comparison of compressive failure of cuboidal specimens of (a) a lightly compacted composite (*l*-T-1) and (b) a heavily compacted composite (*h*-L-1) that failed by delaminating.

3.1.2 Tension Tests

Uniaxial tension test data are summarized in Table 6 and representative load-strain histories are shown in Fig. 8. The strains of Table 6 and Fig. 8 were measured by a clip gauge of 1 cm gauge length attached to one of the machined sides of the specimen. The output of the clip gauge was the controlled displacement during the test. Nonlinearity is evident at stresses over half the peak load for both lightly and heavily compacted composites. However, whereas nonlinearity sometimes appears to be reversible, elastic deformation in compression, in tensile loading it is associated with resin microcracking. The heavily compacted materials are far stronger than the lightly compacted materials, with strengths often exceeding 1 GPa. The strains to failure are ostensibly large, much higher than those of 2D laminates, but the quoted numbers and the abscissae of Fig. 8 should be interpreted with care. They do not reflect material constants, but are strongly influenced by whether large tensile cracks fall within the clip gauge field, as discussed below.

Table 6

Tension Test Data—Loading in Stuffer Direction

Preform Label	Peak Load (MPa)	Measured Modulus (GPa)	Strain to Failure[a]	Rule of Mixtures Modulus[b] E_x (GPa)
l-L-1	300 ± 50	30 ± 6	0.015 ± 0.005	36
l-L-2	240 ± 10	28.5	0.03 ± 0.01	41
l-T-1	350	27	0.04	48
l-T-2	240	39	0.02	49
l-O	390 ± 30	30 ± 2	0.022 ± 0.002	51
h-L-1	980 ± 20	85 ± 8	0.018	96
h-L-2	935	80	0.039	85
h-T-1	840	79	0.038	92
h-T-2	895	72	0.013	89
h-O-1	1070	88	0.013	96
h-O-2	850	69 ± 5[c]	0.013 ± 0.001	86

[a] Interpret with caution! See text.
[b] From Eq. (3), with $A_S = f_S$.
[c] Bilinear stress-strain curves: the figure shown for the modulus is the average over the whole range of the test.

Detailed examinations of tensile failure mechanisms were made for all composite types. Photographs of gauge sections taken during tests were examined by stereoscopy to reveal relative displacements across cracks, strain fields in intact regions, and overall pictures of damage. The principal damage events in both the lightly and heavily compacted composites are matrix cracking (both tensile and delamination), tow rupture, and tow pull-out.

The main load drops observed in stress-strain records, e.g., Fig. 8, were caused by the rupture of one or more aligned tows. When a tow ruptures, it almost always fails across its entire cross-section. Matrix cracking around the circumference of the failed tow then debonds it from the surrounding composite, so that any stress concentration is minimized and neighboring aligned tows commonly remain intact. Sliding along circumferential debond cracks typically extends several mm from the location of the rupture.

The rupture of an aligned tow is also associated with matrix cracking that separates fillers, which are the orthogonally disposed tows in the current experiments (Fig. 9). Inspection of specimen sections reveals that such interfiller cracks begin at strains exceeding ~ 0.6% for lightly compacted composites and ~ 1% for heavily compacted composites. They become widespread after

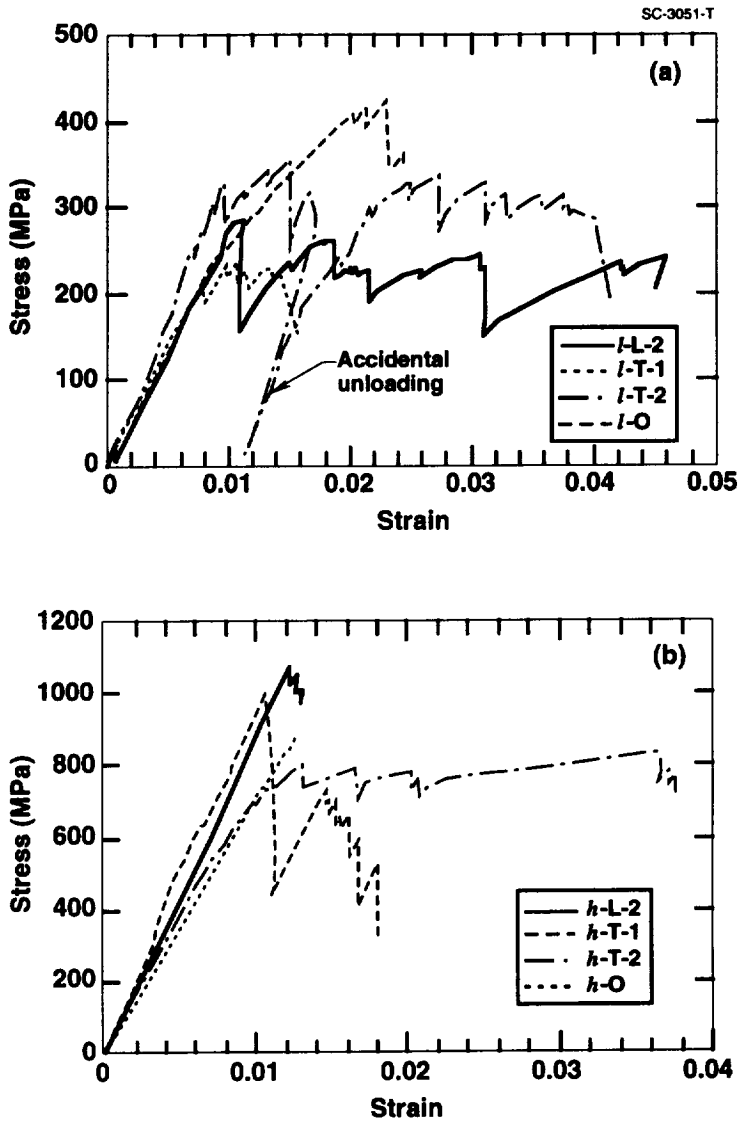

Fig. 8 Stress-strain records for dogbone specimens of (a) lightly compacted and (b) heavily compacted composites under unaxial tension.

loading to high strains in all specimens studied, with the unexplained exception of the lightly compacted material *l*-O. The layers of resin between fillers are clearly much weaker than the fillers themselves, since the fillers are rarely seen to fail internally. The interfiller cracks are analogous to the multiple cracks found in the 90° plies of 0°/90° laminates, *except that their spacing is dictated by the filler size rather than the mechanics of stress relief.*

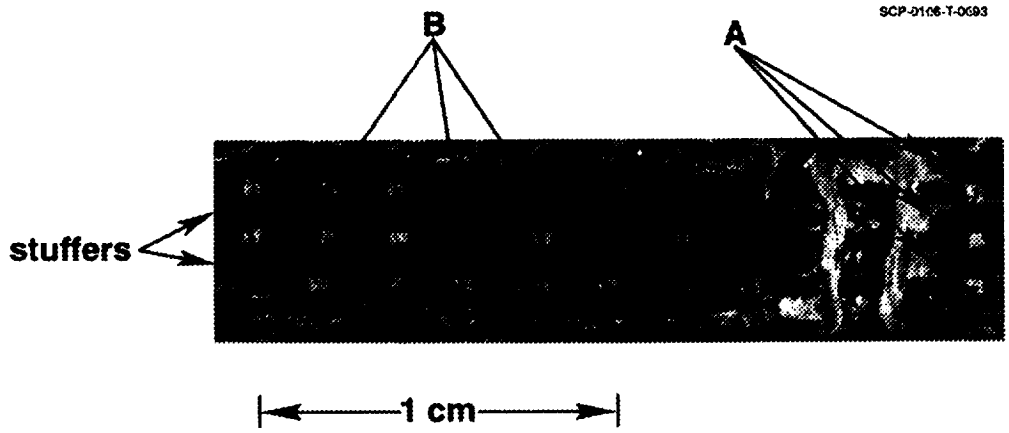

Fig. 9 The separation of fillers under tension in the stuffer direction in an orthogonal interlock composite (*h*-O-1). Arrow at A shows simple fracture between fillers. Arrows at B show instances of fracture followed by falling away of pieces of resin.

As the number of ruptured stuffers increases, interfiller cracks on one or more planes develop large openings, until a macroscopic "tension crack" is evident (Fig. 10). Such tension cracks may traverse the whole specimen, but since stuffer failures are not generally coplanar, they remain bridged by intact stuffers. One tension crack will commonly cause ultimate failure when the bridging stuffers fail and are pulled out of the fracture surfaces (Fig. 10). Tension cracks that have been caught within the field of view of photographic records may have opening displacements of several tenths of a mm when the load is still near the peak load. Pullout distances for bridging stuffers may exceed 1 cm. The case of Fig. 10b shows broken tows that sustained weak pullout loads when the total displacement equalled the length of the specimen gauge section.

Tension cracks do not always cross the whole specimen. When viewed on a cut side of the specimen, they are seen occasionally to terminate at a delamination crack running parallel to the load axis between a layer of stuffers and a layer of fillers. Ultimate failure may then consist of separation of the specimen along a path comprising the first tension crack, the delamination crack, and a second tension crack traversing the rest of the specimen. The two tension cracks may be offset from one another by ~ 1 cm. More complex systems of tension and delamination cracks might be expected in large specimens and are common in bending (see below). Reciprocally, when the failure path involves delamination and offset tension cracks, specimens under uniaxial loads develop local bending because of broken symmetry.

The strains reported in Table 6 and Fig. 8 will obviously depend strongly on whether or not a tension crack falls within the field of the clip gauge extensometer. If one does, then high

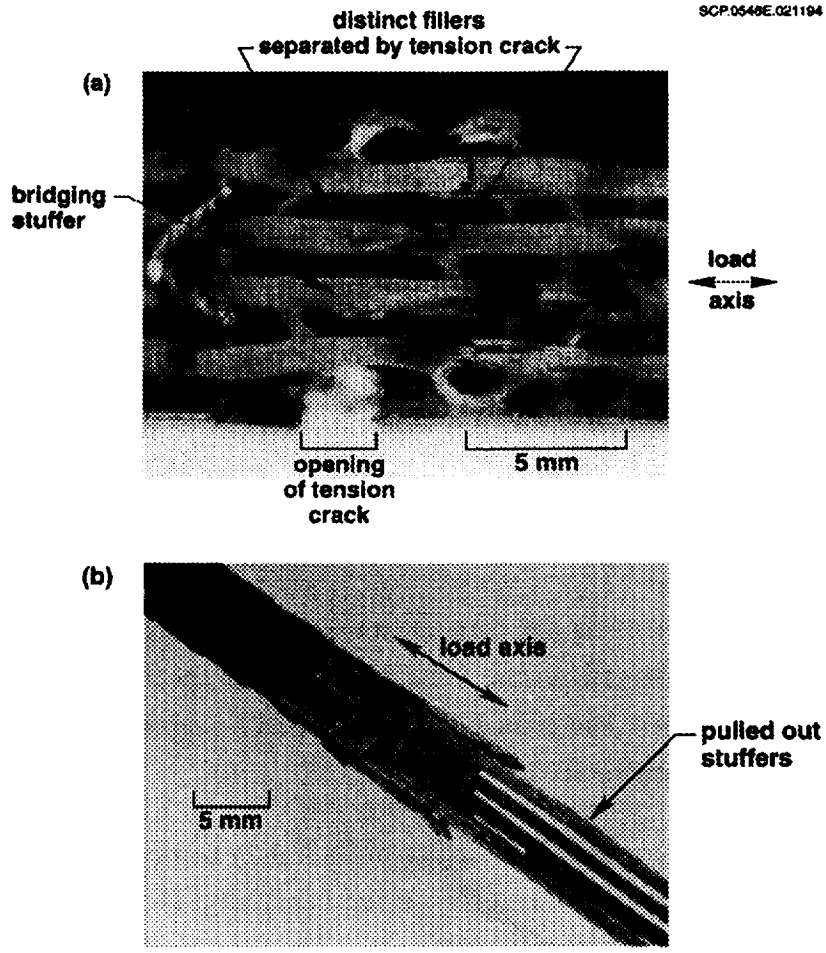

Fig. 10 (a) A lightly compacted composite (*l*-T-1) and (b) a heavily compacted composite (*h*-O-1) after testing in uniaxial tension.

strains to failure will be recorded. If not, the measured strain may actually decrease when a tension crack forms elsewhere and relieves the load. In this case, truncated stress-strain curves result, such as those for materials *h*-L-2 and *h*-O in Fig. 8(b). Thus the strains to failure quoted in Table 6 should not be regarded as material constants, but merely suggestive of high damage tolerance. A meaningful quantification of damage tolerance should be based on laws for tow pullout (vide infra).

While stuffers account for most of the composite strength in the orientation chosen for the experiments, significant bridging of tension cracks may also be supplied by warp weavers. Because they are initially curved, warp weavers qua bridging ligaments are relatively soft, but survive high crack opening displacements.

Matrix cracks form not only normal to the applied load, but also to a lesser extent at other angles under the influence of the local orientation of tows. Significant matrix cracking is usually found prior to any stuffer failures, typically at loads above half the peak load, and is correlated with macroscopic softening.

There is some evidence of residual stresses in the matrix. Sensitive strain measurements* reveal net compressive strains in the matrix in unloaded cracked specimens relative to the same specimens when unloaded and undamaged, which suggests that the cracks have allowed partial relaxation of tensile residual stresses. The relaxation of residual stresses is also thought to be responsible for the observed normal opening of delamination cracks that lie parallel to the load axis.

3.1.3 Bending Tests

In the presentation of bending test data, all stresses and strains refer to those that would exist in the outer layer of material on the tensile side of the specimen if the material was homogeneous, given the load and load point displacement. Some simple remarks on the effects of inhomogeneity on strength follow in Section 3.2.

Figure 11(a) shows a four-point bending test of a lightly compacted layer-to-layer angle interlock specimen. Failure began at the center of the beam with kink band formation on the compressive side followed by tow rupture on the tensile side. Very limited delamination occurred on the tensile side only. The material exhibits considerable ductility. Figure 11(b) shows three-point bending data for the same material. As indicated in the figure, the main load drops are correlated with the kinking and rupture of stuffers. Once again delamination is very limited.

Four-point bending tests of some heavily compacted materials were spoiled by extensive delamination between the outer loading pins. Since shear was evidently a principal failure mode for these composites, all further tests were conducted in three-point bending. With some variance from test to test duly noted, representative load-strain records are shown in Fig. 12, where significant load drops are annotated with corresponding observations. Of the heavily compacted materials, both the layer-to-layer angle interlock (Fig. 12a) and orthogonal interlock (Fig. 12b) types showed significant delamination, although it was less in the latter. Both types of through-the-thickness angle interlock (Figs. 12c and 12d) showed no significant delamination. Where delamination occurred, it frequently ran from the center of the beam all the way to one end and was always

* Stereoscopy and automated differential displacement analysis. See [11] and [12] for details of these methods.

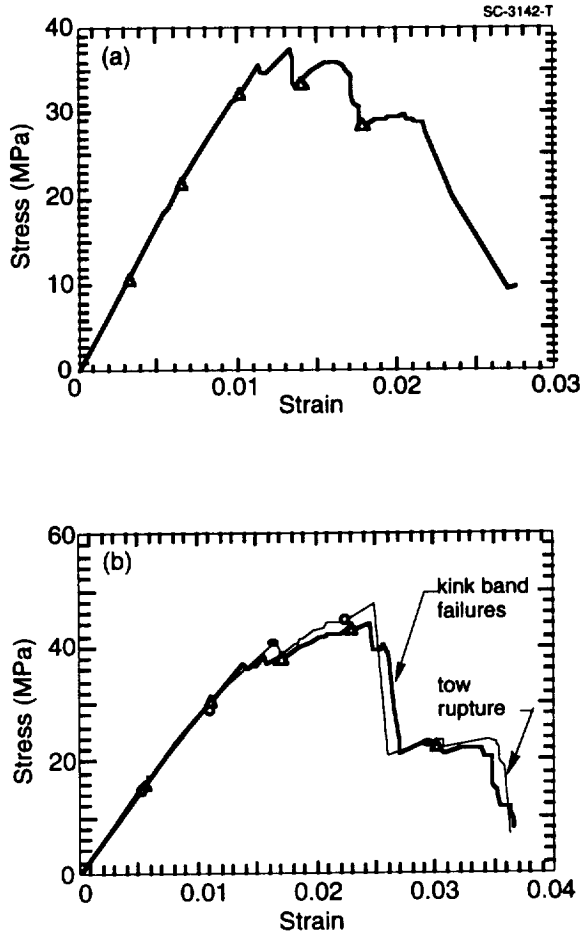

Fig. 11 Test results for lightly compacted layer-to-layer angle interlock specimens (type *l*-L-1 of Table 1) in (a) four-point bending and (b) three-point bending.

accompanied by a large load drop. Shear displacement discontinuities of up to 1 mm are commonly observed across delaminations that have run the specimen, yet the delaminations remain bridged by intact warp weavers (Fig. 13). Some striking periodic patterns were produced on the upper and lower surfaces of the specimen in such cases, where the near-surface extremities of bridging warp weavers have been pulled down strongly into the body of the composite (Fig. 13).

In summary, bending tests reveal much the same failure mechanisms for stuffers as uniaxial tests, namely kink band formation on the compressive side followed by tow rupture on the tensile side. In correspondence with behavior under unaxial compression, the strain to failure in bending tends to be larger for the lightly compacted composites than for the heavily compacted composites. Substantial delamination does not occur in lightly compacted composites in bending. Whether it occurs in heavily compacted composites depends on the reinforcement architecture.

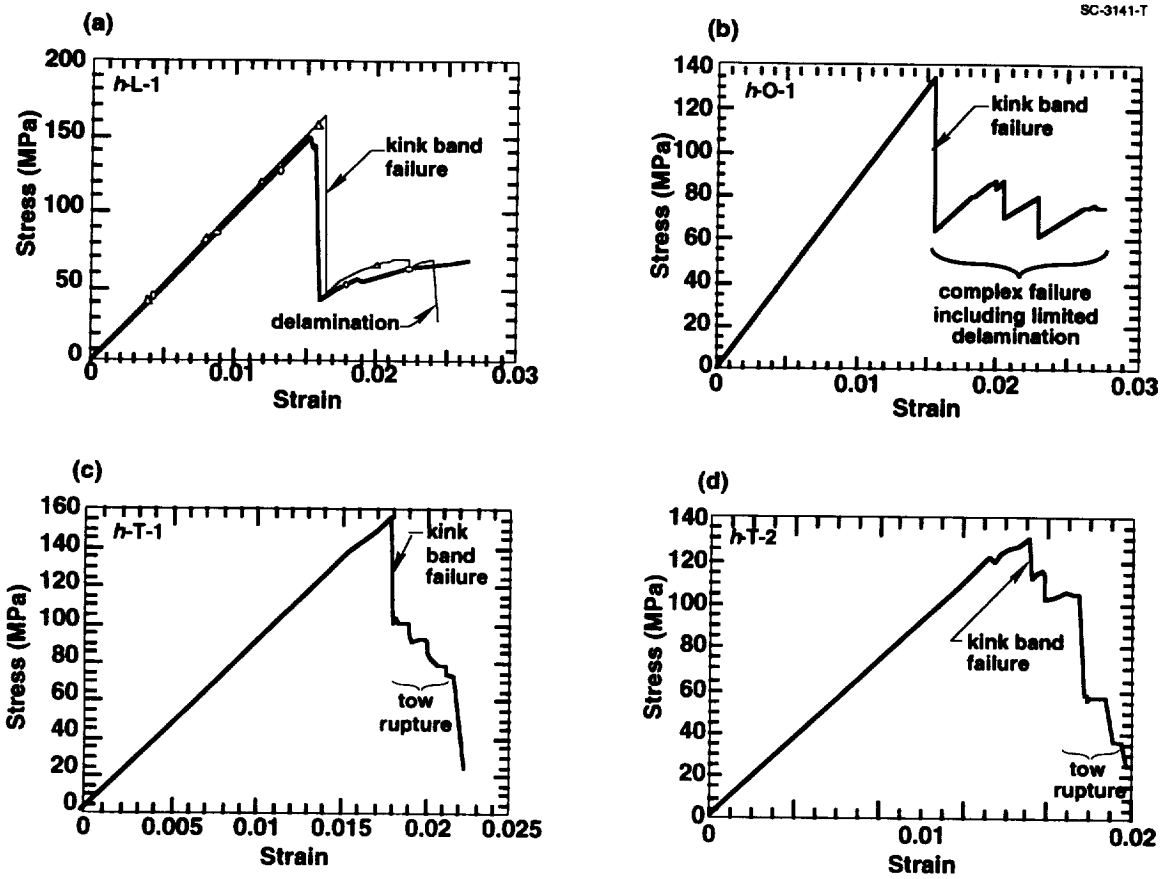

Fig. 12 Test results for various heavily compacted composites in three-point bending.

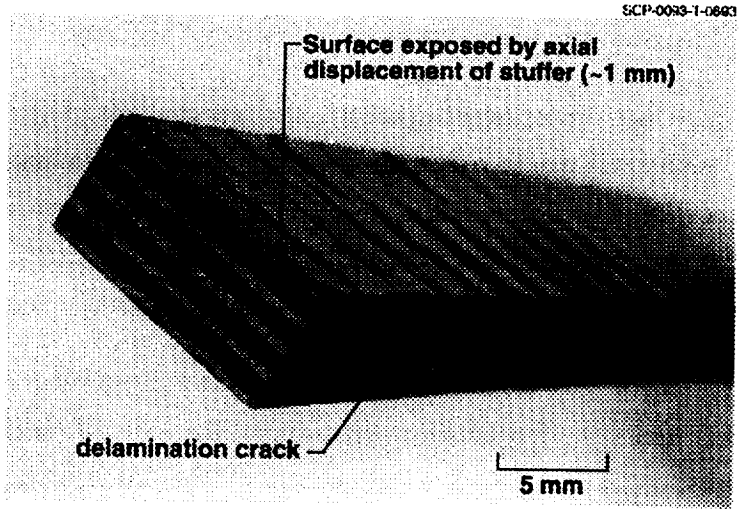

Fig. 13 A delamination crack created in a specimen of type *h*-O-1 by three point bending, with large mode II crack opening displacement. The upper surface shows systematic damage caused by warp weavers that bridge the delamination crack.

3.1.4 Compression After Impact

Tests of compressive strength after impact were made for some of the heavily compacted composites. Rectangular specimens were impacted by Professor George Springer and colleagues at Stanford University. The impact was effected by a Teflon projectile fired by an air gun. Several velocities were used and the damage produced probed by x-ray radiography. A circular zone of damage of about 1 cm in diameter was found for the highest velocity, which corresponded to an impact energy of ~ 10 ft-lb (13.5 Nt-m).

Table 7 compares residual strengths after impact with the data for pristine dog-bone specimens. Ignoring the case that terminated prematurely via Euler buckling, the loss of strength is ~ 20%. This is close to the reduction that would be expected from net section considerations. The impact damage affects stuffers within a volume of width approximately 1 cm and depth approximately 2 mm, while the impacted specimens were approximately 2.5 cm wide and 0.5 cm thick. If all stuffers within the impact zone are assumed to have zero strength and stiffness, the average load on the remaining stuffers must rise by a factor $1.25/1.05 \simeq 1.2$. Thus the strength should fall by ~ 20%. Further justification for using net section estimates appears in Section 3.2.3.

Table 7

Compression After Impact

Composite Label	Pristine Strength[a] (MPa)	Compressive Strength After Impact[b]
h-L-1	670	345[c]
h-T-1	570	510
h-T-2	540	435
h-O-1	635	470

[a]From Table 5 - dog-bone specimens.
[b]10 ft-lb (13.5 Nt-m) applied by Teflon projectile.
[c]Specimen failed by Euler buckling.

3.2 Theoretical Estimates of Properties

3.2.1 Modulus

Reasonable estimates of Young's modulus in the loading direction (i.e., the direction of the stuffers) can be found by appropriate rules of mixtures. For this purpose, it is expedient to separate fibers into those lying in stuffers and all others, not discriminating fillers and warp weavers among the latter. Let V be the volume fraction constituted by all fibers and f_s the fraction of all fibers that lie in stuffers. If A_s is the area fraction occupied by stuffers on a section normal to the load axis, then the axial Young's modulus, E_s, for a stuffer is by rule of mixtures

$$E_s \simeq \frac{f_s V}{A_s} E_f + \left(1 - \frac{f_s V}{A_s}\right) E_r \ , \tag{1}$$

where E_f is the axial modulus of the fibers and E_r the modulus of the resin, which is assumed isotropic. The remaining resin and fibers, i.e., those in the fillers and warp weavers, may be considered to form an effective medium whose modulus, E_m, may be approximated in the direction parallel to the stuffers by*

$$E_m \simeq \left[\frac{(1-f_s)V}{1-A_s}\frac{1}{E_f} + \left(1 - \frac{(1-f_s)V}{1-A_s}\right)\frac{1}{E_r}\right]^{-1} \ . \tag{2}$$

Young's modulus, E_l, of the entire composite in the direction of the stuffers is approximately

$$E_l \simeq A_s E_s + (1 - A_s) E_m \ . \tag{3}$$

If $E_f >> E_r$, as for graphite/epoxy composites, the dominant term in E_l is thus $f_s V E_f$, which is independent of A_s. This has practical importance, because it is often difficult to assign an area fraction to stuffers when examining cross-sections of composites. The cross-sections of stuffers and indeed all tows are often heavily distorted and variable; and measuring A_s is further complicated by resin-rich regions between tows. On the other hand, V can be measured accurately by acid digestion, while f_s is known accurately from the records of the weaver. Since E_l is weakly dependent on A_s/f_s for feasible values of A_s, it is expedient here to use the approximation $A_s = f_s$.

* Equation (2) is a reasonable approximation for fillers, which are loaded transversely by loads parallel to the stuffers. Warp weavers, on the other hand, lie roughly at 45° to the stuffers and might be thought to offer stiffer resistance than intimated by Eq. (2). However, warp weavers constitute a relatively small volume fraction and their effective modulus is often reduced by crimping. Thus the error should be minor.

Using the manufacturer's datum E_f = 250 GPa for AS4 fibers, the values E_r = 3.5 GPa for the Shell 1895 resin and E_r = 2.8 GPa for Taxtix 138 with H41 hardener (both measured by the authors), and the fiber volume fractions of Table 2 with $A_s = f_s$, one finds from Eq. (3) the estimates of E_x for loading in the stuffer direction that are shown in the right-hand column of Table 6. (In estimating E_1 for composites *l*-L-2 and *l*-T-2, the significance of having S-2 glass rather AS4 warp weavers was assayed by letting the modulus for the S-2 glass warp weavers be either zero or equal to that of AS4 fibers. The values so computed for E_1 differed by less than 1%; which one would expect since the warp weavers have low volume fraction and influence E_1 via the relatively small term E_m only.) The estimates are 20-50% higher than the experimentally measured values for the lightly compacted composites and 10-20% higher for the heavily compacted composites. These discrepancies are consistent with rough estimates of the effects of the stuffer waviness noted in Section 2. Waviness leads to lower effective moduli, because the reaction of a wavy tow to an aligned load is not merely to extend but also to straighten.

3.2.2 Strength

Compression

Kink band formation in fibrous polymer composites is mediated by shear deformation of the matrix [13,14]. Under the simplest assumptions concerning the geometry of the kink band, the critical axial stress for kinking, σ_k, is given by [13-15]

$$\sigma_k = \tau_r/\phi \quad , \tag{4}$$

where τ_r is the critical stress for shear flow in the resin and ϕ is the angle by which the fibers are misaligned with respect to the applied load axis. Equation (4) obtains for an infinite array of uniformly misaligned fibers, whereas the kink bands of interest here exist within single, finite tows whose misalignment varies continuously and randomly along their length. The extent to which such details influence the criterion for kinking has not been studied. With such doubts set aside in the spirit of identifying trends, some useful numbers emerge when measured values of τ_r and ϕ are substituted into Eq. (4).

The critical shear stress, τ_r, was deduced to be ~ 75 MPa from tension tests on ±45° laminates (see Appendix B). The misalignment angle ϕ was measured on photographs of stuffers exposed on several sections cut perpendicular to the filler direction, since the most severe stuffer deflections always occur normal to fillers. The sections revealed all the stuffers in a volume of material approximately equal to that of the gauge section in dog-bone tests (as in Fig. 5). Since

there are rarely more than two load drops prior to peak load in compression tests, the attainment of peak load was somewhat arbitrarily equated to the occurrence of the second kink band. Thus the angle ϕ corresponding to peak load was taken to be the second greatest misalignment angle measured anywhere in a given set of sections. The results of these procedures are shown in Table 8. The critical value, $\sigma_a^{(k)}$, of the applied stress at which kink bands first form is related to σ_k by

$$\sigma_a^{(k)} = \frac{E_l}{E_t}\sigma_k \simeq A_s\sigma_k \ , \tag{5}$$

where A_s is the area fraction constituted by stuffers on planes normal to the stuffer direction, which can be approximated by the fiber fraction f_s of Table 2. The values of $\sigma_a^{(k)}$ are encouragingly consistent with the experimental results of [9] and Tables 3 and 4, reinforcing the view that kink band formation is the essential mechanism of failure.

Table 8

Estimates of First Kink Band Formation

Material	τ_r (MPa)	ϕ (radians)	$\sigma_k = \tau_r/\phi$ (MPa)	A_s	$\sigma_a^{(k)} = A_s\sigma_k$ (MPa)	Measured Ultimate Strength[a] (MPa)
l-L-1[b]	75	-	-	-	-	-
l-L-2	75	0.21	380	0.385	140	150±10
l-T-1	75	0.23	350	0.41	135	155±5
l-T-2	75	0.17	460	0.38	165	200±5
l-O	75	0.26	300	0.39	110	-[b]
h-L-1	75	0.052	1520	0.58	850	670
h-L-2	75	0.087	915	0.58	495	695
h-T-1	75	0.087	915	0.57	485	570
h-T-2	75	0.087	915	0.59	505	540
h-O-1	75	0.070	1145	0.59	635	635
h-O-2	75	0.070	1145	0.54	575	555±15[c]

[a] From Tables 4 and 5.

[b] Not measured.

[c] Experiment gives a lower bound for $\sigma_a^{(k)}$, since failure was by Euler buckling.

Tension

The manufacturer quotes a strength of 4 GPa for AS4 fibers.* The stress, σ_s, in the fibers in the aligned tows (stuffers) is approximately related to the applied stress σ_a by

$$\sigma_s \simeq \frac{E_f}{E_l}\sigma_a \quad , \tag{6}$$

with E_l given by Eq. (3). For the values given above for E_f and the estimates of Table 6 for E_l, Eq. (6) would imply that tow rupture should occur at tensile stresses of 500-700 MPa for the lightly compacted composites and ~ 1.5 GPa for the heavily compacted composites. In fact, the measured composite tensile strengths are roughly half to two-thirds of these estimates (Table 6). There are several likely causes of strength degradation. 1) Prior to weaving, AS4 yarns are wrapped with polyvinyl alcohol threads to prevent spreading. The polyvinyl alcohol is removed with hot, distilled water when the weaving is completed. Some chemical degradation of the fibers is possible. 2) The rigors of the weaving process are always likely to damage tows. 3) As shown in Section 2, both the weaving and consolidation processes result in deformation of tows. Nominally aligned tows that are not straight will have a lower effective modulus, leading to overloading of neighboring tows that are straight. 4) A misaligned, kinked, or nonuniformly squashed tow may be weaker than a straight tow. 5) Lateral loads are induced on aligned tows by the reaction of warp weavers to in-plane tension, which may reduce their strength.

Some of these factors also differentiate 2D laminates of plain weave fabric and conventional, nonwoven 2D laminates. Prior studies of graphite/epoxy composites in these classes have shown that the strength of 2D woven laminates under loads aligned with the warp tows is 15-25% lower than in comparable 0°/90° laminates, while differences in fiber volume fraction are only ~ 10% [16]. Further research is required to determine which factors account for the strength reduction in 3D woven composites being considerably greater than this. For the moment it is enough to say that existing 3D woven composites are probably far from optimal in tensile strength.

Bending

The ratio of the average stress σ_s', in the outermost layer of stuffers in pure bending to the nominal stress, σ^{surf}, quoted in Figs. 10 and 11 is approximately

---

* Data sheets of Hercules, Inc., Wilmington, Delaware.

$$\frac{\sigma_s'}{\sigma^{surf}} = 1 - 2\frac{t_f}{t} - \frac{t_s}{t} \quad , \tag{7}$$

where t_s is the thickness of a stuffer ply, t_f is the thickness of a filler ply, and t is the specimen thickness. The ratio of the ply thicknesses is approximately

$$\frac{t_f}{t_s} = \frac{n}{n+1}\frac{f_f}{f_s} \tag{8}$$

while

$$n\,t_s + (n+1)\,t_f = t \quad , \tag{9}$$

where n is the number of layers of stuffers. For the values of f_s and f_f in Table 2, Eqs. (7) through (9) yield $\sigma_s'/\sigma^{surf} \simeq 0.7$ for the composites for which n = 4 and 0.8 when n = 6.

Multiplying the peak loads in Figs. 11 and 12 by these values of the ratio σ_s'/σ^{surf} provides estimates of the local compressive stresses at which kink bands formed. The resulting stresses, shown in Table 9, are remarkably higher than the ultimate strength under *uniaxial* compression in all cases (Tables 3-5).

Table 9

Critical Compressive Loads in Bending Tests

Preform Label	Critical Value of Nominal Surface Stress (MPa)	Critical Value of Estimated Stress in Outermost Stuffer[a] (MPa)
l-L-1	285 ± 25	200 ± 20
h-L-1	1035 ± 35	725 ± 25
h-T-1	1070	750
h-T-2	895	625
h-O-1	930	650

[a] from Eq. (7)

Similarly high compressive strains in unidirectional graphite/epoxy composites under bending have recently been reported elsewhere [17]. In [17], the possibility was considered that the high compressive strains might be enabled by constraint of microbuckling by the curvature

induced by bending. This mechanism was ultimately rejected in [17] on the grounds that microbuckling should occur in the plane of the surface, rather than out of the surface; it would be unaffected by the curvature of the specimen and would therefore occur at the same lower stress that would be expected for uniaxial loading. However, the universal observation for the 3D woven composites studied here is that microbuckling of near-surface stuffers does involve deflections out of the surface. For the orientation in which specimens were tested here in bending, in-plane deflections of stuffers on the compressive surface of the specimen would have to occur in the weft direction and would therefore be strongly resisted by fillers.

The simple expression of Eq. (4) for kink band formation was derived for an infinite array of fibers. No analogous criterion is available to account for the presence of a free surface. However, one might conjecture that buckling of a stuffer out of a surface, a precursor to kinking, will occur most readily at locations where tow waviness lends the stuffer maximum convex curvature when viewed from outside the specimen. This conjecture is supported by moiré interferometry of woven composites in uniaxial compression. Such figures show segments of stuffers arching out of one specimen's surface at locations where kinking subsequently occurred. In bending, the curvature of any tow segment will become the sum of that associated with tow waviness and the *concave* curvature produced on the compressive surface by the applied load. The maximum convex curvature in a given specimen will be reduced. The stress required to force some segment of a tow to arch out of the specimen will thus be raised; and if such arching is a prerequisite for kinking, the critical stress σ_k will also be raised. Further work is required to test this conjecture.

3.2.3 Ductility and Notch Sensitivity

Since it dealt with the failure of individual aligned tows in the stress field of an undamaged composite, the discussion of the previous section pertains strictly to the critical stress, in either compression or tension, for *isolated* tow failures. How the material progresses thence to ultimate failure depends on the distribution of flaws and how loads are redistributed around the site of each local failure event. The possibility of composite strength exceeding the stress of first tow failure, high strain to ultimate failure, and notch insensitivity are all favored by flaws that are widely distributed both spatially and in strength and by mechanisms of stress relaxation around each tow failure site.

In compression, the essential flaws are geometrical in nature, comprising random misalignments, which are reflected in ϕ in Eq. (4), and certain topological characteristics of the

reinforcement, which cause lateral loads in aligned tows. Lateral loads knock down the critical stress for kink band formation [14,15]. Kink bands are most commonly observed where misalignment is greatest and often near configurations such as that depicted in Fig. 2. (Whether the correlation of kink bands with the deformity of Fig. 2 is attributable to lateral loads or whether it arises wholly because tows are exceptionally misaligned there is impossible to tell from the experimental observations made so far.)

In tension, the nature of the essential flaws has not been established. Geometrical irregularity may be a factor, as surmised in the preceding section, but the mechanics of such effects have not been studied. Whereas kink band formation in compression is not influenced to first order by the inherent properties of the fibers [e.g., 13-15], that is not so of strength in tension. Inherent fiber variance will lead by itself to a Weibull distribution of tow strengths.

Stress redistribution around a site of tow failure has now been observed in both compression and tension to be moderated by debonding of the failed tow from the surrounding composite. Accurate strain mapping by stereoscopy reveals large discontinuities in the axial displacement across the debond. It is likely that the implied sliding is governed by friction. The observed sliding lengths are typically many times the tow diameter, which invites analysis by the usual, simple shear lag theory. Let τ_f denote the critical shear stress at which sliding is activated. Assuming τ_f to be uniform over the debond and that the kind band supports negligible axial load, the sliding length, l_s, satisfies

$$s l_s \tau_f = \sigma_t A \quad , \tag{10}$$

where s and A are the circumference and cross sectional area of the tow and σ_t is the axial stress it bears beyond the sliding zone. The degree of stress concentration in tows neighboring a failed tow diminishes with increasing sliding length and therefore increases with the magnitude of τ_f . In a 3D composite, τ_f will be strongly influenced by triaxial local stresses generated even under uniaxial loading by the through-thickness reinforcement (warp weavers). For fixed τ_f, the sliding length also increases with the tow denier, which is reflected in Eq. (6) by the ratio A/s. *The fact that large slip distances are observed in the subject 3D composites is thus a direct consequence of the coarse scale of the reinforcement.*

Tension

In the tensile tests reported above, ultimate failure was associated with a band of damage traversing the specimen. The band can be viewed as a dominant crack bridged by tows being

gradually pulled out of its fracture surfaces (e.g., Figs. 9a and 9b). In all the tests reported here, this crack spanned the specimen as soon as it was observable. However, for a sufficiently large specimen, one might envisage such a bridged crack emanating a limited distance from a stress concentrator such as a hole. The response of the material will then depend on the nature of the bridging or cohesive zone. The detailed mechanics of the failure process are complex and computationally challenging, but the essence will be as schematized in Fig. 14.

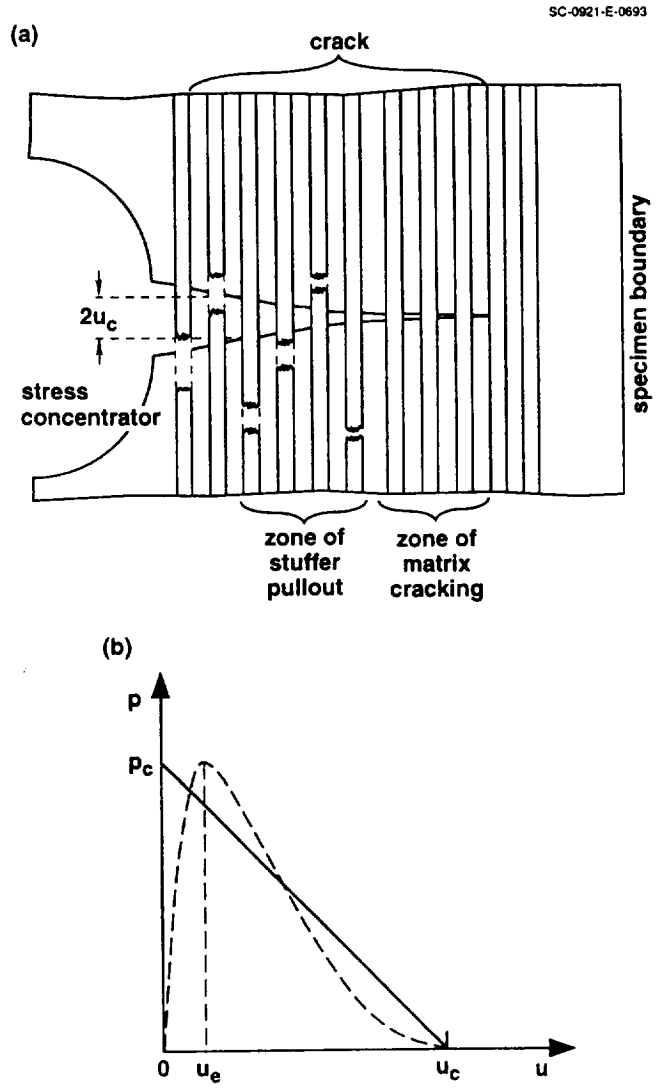

Fig. 14 (a) Conjectured distribution of damage in a large specimen under tension. (b) Conjectured tractions acting over central damage plane vs crack opening displacement (or half the displacement discontinuity across the damage plane).

Figure 14a shows a process zone consisting broadly of two parts. Furthest from the stress concentration, damage will consist of interfiller cracks between intact stuffers, a "zone of matrix cracking". Nearer the stress concentrator, stuffers will have failed. Since the stuffer failures will not all coincide with the main fracture plane, a "zone of tow pullout" will exist, within which failed stuffers continue to transfer loads via friction. When the damage has propagated far enough, the stuffers nearest the stress concentrator will pull entirely out from one fracture surface, forming a traction free zone.

The fracture mechanics of this crack system are determined by the relation between the tractions p acting across the crack and the crack opening displacement u (or displacement discontinuity 2u). The problem is analogous to that of the pullout of fibers of random strength from a brittle matrix composite [18,19]. Qualitative analysis leads to a relation p(u) schematized by the dashed curve of Fig. 14b. In the zone of matrix cracking, the intact stuffers act roughly as bridging springs, so p(u) will be an increasing function. When $p = p_c$, a value close to the ultimate strength for loading along the stuffers, stuffer failure will commence. The corresponding value u_e of u will be relatively small, because stuffers deform elastically for $u < u_e$. At higher displacements, p(u) will fall monotonically, vanishing when $u = u_c$ at the trailing end of the zone of tow pullout.

In describing the extension of a single band of damage from a stress concentrator, the brief rising part of p(u) has no significant role. (Material properties that do depend on the rising part of p(u) are reviewed in [20]). Since $u_c >> u_e$ for the composites studied here, p(u) can be idealized by the solid line in Fig. 14b.

The fracture process could also in principle be influenced by the work required to advance the zone of matrix cracking, i.e., to form new interfiller cracks. However, this energy is much smaller than that required to pull out failed stuffers. This suggests the closure condition that no stress singularity should exist at the tip of the zone of matrix cracking. The much studied cohesive zone model with tension softening cohesive forces then results.

In such cohesive zone models, a fundamental role is played by the characteristic length, l_{ch}, defined by [21-23]

$$l_{ch} = \frac{u_c E_c}{p_c} \quad . \tag{11}$$

The length of the cohesive zone is given to order magnitude by l_{ch}. When the specimen width is less than l_{ch}, the material will be notch insensitive, with the ultimate strength approximated by the condition that the net section stress should equal p_c (e.g., [23,24]). In large specimens, notch sensitivity exists only for notches much larger than l_{ch}.

Estimates of E_c, u_c, and p_c for the subject woven composites and the resulting values of l_{ch} are shown in Table 10. The values of E_c are taken directly from Table 4. The estimates of p_c are the strengths of Table 4. The ranges shown for u_c correspond to the range of measured tow pullout lengths. The resulting values of l_{ch} are substantial fractions of 1 m. If such high values are realized, then in all practical applications, these materials will be notch insensitive and damage tolerant under tensile loads.

Table 10

Estimates of Cohesive Zone Lengths for Tension Cracks

	E_c (GPa)	u_c (mm)	p_c (GPa)	l_{ch} (cm)
Lightly Compacted Composites	30	1-5	0.3	10-50
Heavily Compacted Composites	80	1-5	0.9	10-50

The length l_{ch} will be reduced if the effective pullout length is reduced. The pullout length will decrease if the distribution of flaw strengths decreases in width, vanishing when all tows fail at a single strength [18,19]. If tow rupture and sliding are accompanied by disintegration of the surrounding composite, bridging tractions will be lost at smaller tow displacements and the effective pullout length will again be reduced.

If u_c is reduced by a factor of 10 from the lower end of the estimated ranges of Table 10, then significant notch sensitivity would arise in practical applications.

On the other hand, damage tolerance in tension can be enhanced by appropriate composite design. The critical displacement u_c and therefore l_{ch} can be made large by 1) using coarse reinforcement (large tow denier) and 2) building in spatially distributed flaws in aligned tows. In the latter regard, the conjecture that tow tensile strength is lowered by lateral loads (which can be imposed intentionally through the choice of weave architecture) is worth pursuing. Rarely has a class of materials promised such scope for tailored properties.

Compression

The high compressive strains to failure measured in lightly compacted composites contrast with the brittleness of stitched quasi-isotropic laminates [9]. The principal distinction between the two groups of materials lies in the distribution of flaws. Stitched laminates are heavily compacted and the laminas in them are relatively flat and well aligned. The critical stress for kink band formation is therefore relatively high and such geometrical flaws as exist are distributed narrowly in strength. Consequently, the first kink failure occurs usually in an outside ply at a stress near the critical stress for kinking of its neighbor. The stress concentration around the first failed ply causes immediate failure of the neighbor; and so the damage propagates unstably across the specimen. In the lightly compacted 3D woven composites, geometrical flaws are distributed broadly both spatially and in strength. The first tow failure is generally associated with a severe flaw. The resulting stress concentration may not suffice to fail neighboring tows, which may have no major flaws in that vicinity. The next failure event is then at a distant site uncorrelated with the first; and so damage accrues in a spatially distributed fashion and the material is ductile.

The heavily compacted composites are appreciably more regular than the lightly compacted composites. Heavy compaction has minimized distortion of stuffers, the principal load bearing tows. However, residual distortions such as those depicted in Fig. 2 still constitute geometrical flaws more severe than those found in stitched laminates. Consequently, one would expect the heavily compacted composites to display damage tolerance and ductility in compression lying between those of the lightly compacted composites and stitched laminates. This is indeed the case.

Compressive strength, on the other hand, is likely to be degraded by geometrical irregularity. Table 11 compares the ratio of compressive strength to fiber volume fraction for the lightly and heavily compacted composites. In composites of equal irregularity, this ratio would be expected from Eqs. (4) and (5) to be constant. It tends to be much greater for heavily compacted than for lightly compacted composites.

Thus the lightly and heavily compacted composites demonstrate an essential balance in the properties of woven composites. While reduced geometrical irregularity in the latter leads to higher compressive strengths than would follow from consideration of volume fraction alone, this comes at the price of reduced strain to failure in compression.

Table 11

Variation of Compressive Strength with Fiber Volume Fraction

Preform Label	Strength[a]/$f_s V^b$ (GPa)	Preform Label	Strength[a]/$f_s V^b$ (GPa)
l-L-1[c]	1.6	*h*-L-1	1.8
l-L-2[c]	1.0	*h*-L-2	2.1
l-T-1[c]	0.9	*h*-T-1	1.6
l-T-2[c]	1.1	*h*-T-2	1.6
l-O	-	*h*-O-1	1.8
		h-O-2	1.7

[a]Strength for dog-bone specimens.
[b]Product $f_s V$ from Table 2.
[c]Strength from Table 4.

Apart from questions of flaw distribution, compressive failure in the heavily compacted composites is also affected by the occasional observation of delamination and subsequent Euler buckling. This failure mode is not observed in either the lightly compacted composites or in stitched laminates, where any delamination cracks that occur remain small rather than propagating the length of the specimen and there is no buckling of the material on either side of them. A simple model of the role of through-thickness reinforcement in bridging such delamination cracks has been presented in [25] and [26]. Under uniaxial loading, buckling must precede delamination crack growth, since otherwise the specimen remains flat and there is no crack driving force. Through-thickness reinforcement raises the critical stress for buckling by providing an elastic foundation for the material on either side of any delamination crack. If buckling is thus suppressed, the delamination crack will not propagate and failure proceeds via kink band formation.

The efficacy of the through-thickness reinforcement depends on the effective stiffness it supplies in acting as an elastic foundation, which depends on the denier and fiber type of the through-thickness tows and their volume fraction. A lower bound to the foundation stiffness can be calculated by assuming that the through-thickness tows transfer load to the rest of the composite only at their extrema. In stitched laminates or through-the-thickness weaves (preforms whose labels contain T or O in Table 1), the extrema lie at the specimen surfaces. Simple estimates can then be made of the minimum volume fraction required to suppress buckling at loads up to that for failure by kink band formation. This critical volume fraction is independent of the delamination length [25,26]. For current stitched laminates, the stitching density is probably one or more orders

of magnitude greater than required to meet this criterion [26]. In this regard, the stitched laminates are overdesigned.

In woven composites with the volume fractions of Table 2, the same ought to be true [26]. However, the warp weavers in woven composites are distorted during consolidation, especially, as one would expect, in the heavily compacted composites (Fig. 4). The distortion can greatly reduce the effective stiffness of the warp weavers under through-thickness loads: they deform in shear rather than in tension. The degradation is evidently so severe in the heavily compacted composites that the elastic foundation can become too soft to suppress buckling, and failure by kink band formation is sometimes not achieved. Confirmation of this conjecture was sought by measuring the longest delamination crack visible on the sides of specimens subjected to approximately the same applied compressive strain. These measurements are plotted in Fig. 15 against the ratio of the net composite thickness (Table 2) to the average thickness of the dry fiber preform as received from the weaver. The severity of warp weaver crimp seen on sections of specimens is in qualitative correspondence with this ratio. So too is the propensity for delamination, as evident in Fig.15. As expected from differences in constraint, Fig. 15 also shows a tendency for delamination to be more pronounced in dog-bone specimens than in cuboidal specimens. Figure 15 clearly demonstrates the virtue of achieving high fiber volume fraction by controlling the weaving process rather than applying heavy compaction loads during consolidation.

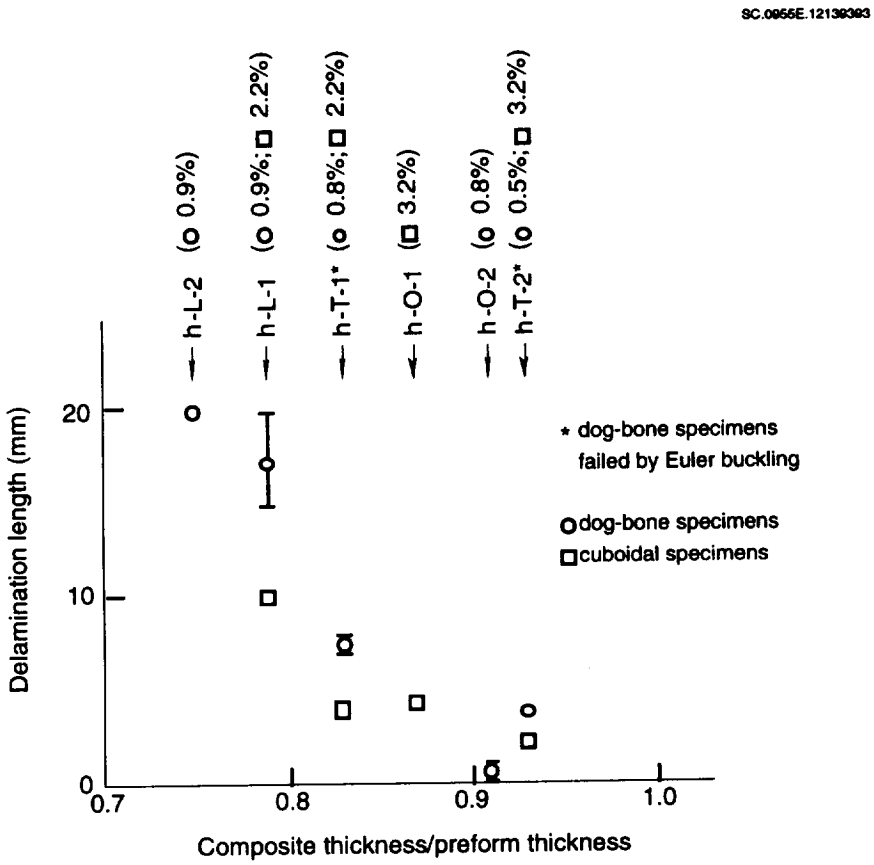

Fig. 15 Maximum delamination crack length observed as a function of the degree of through-thickness compaction achieved in consolidation. The preform type and compressive strains at which measurements were made are marked at the top of the figure.

Compression After Impact

Provided failure occurs by kinking rather than by delamination and buckling, a simple extension of the idea of the cohesive zone used for notch sensitivity in tension could be used to estimate residual compressive strength after impact (e.g., [28]).

Consider the impact damage zone to be a hole, which is an extreme assumption of the damage state and should lead to conservative strength estimates. Upon compressive loading, kinking will propagate out from this stress concentrator, much as tow rupture would progress in tension (Fig. 14a). Bridging tractions, in this case propping the crack open and shielding unkinked stuffers ahead of the damage zone from compressive loads, will arise because of the kink lock-up mechanism discussed below in Section 6 and Appendix D. This amounts to a *compressive* cohesive zone, which will have some characteristic length l_{ch} in analogy to that of Eq. (11). We

have insufficient knowledge of the mechanics of kink initiation and stress redistribution following kinking to make good estimates of l_{ch}. However, our qualitative observations of damage mechanisms suggest that compressive cohesive zones of the order of several cm. are feasible for these coarse woven composites. In that case, the success of net section considerations in estimating strength after impact in Section 3 would be no surprise. The damage zone there was only $\approx$ 1 cm.

Further research on this idea would seem warranted.

4. Fatigue

4.1 Compression-Compression

Strain-life tests were executed under uniaxial, compression-compression loading using dog-bone specimens. Results for lightly compacted composites are shown in Fig. 16, with the data for one cycle being the monotonic data of Table 4.

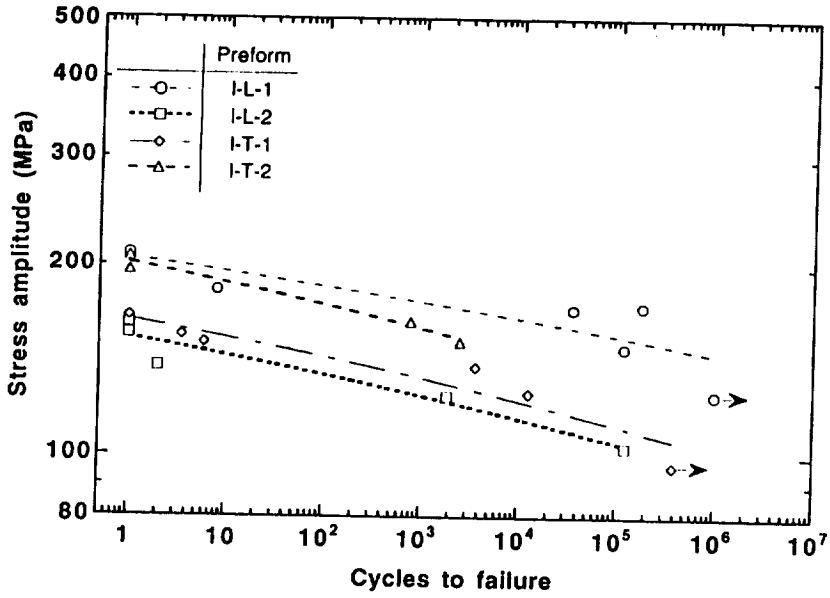

Fig. 16 Stress-life data for lightly compacted woven composites under uniaxial compression-compression fatigue.

Woven composites and stitched laminates have a similar contrast in fatigue to that observed in monotonic loading. A few fatigue tests for stitched laminates showed very flat S-N curves: an increase in load of 10% (from 38 ksi to 42 ksi for the specimens tested) reduced a fatigue life exceeding one million cycles (run-out in test) to failure in one cycle. Figure 16, in contrast, shows significant slope to the S-N curves.

Figure 17 shows stress-life data for four of the high volume fraction (heavily compacted) woven composites supplied by Boeing. The tests show that the orthogonal interlock architecture yields the highest strength, while the layer-to-layer angle interlock architecture yields the lowest strength. This is consistent with our view that angled warp weavers act as geometrical flaws where they wrap around fillers, which can be quantified by measurements of misalignment angles for stuffers. The layer-to-layer angle interlock architecture has the highest misalignment angles; the orthogonal interlock architecture the lowest. However, there is also substantial delamination in some of these weaves during fatigue, apparently depending on the extent to which warp weavers have been crimped during processing. Crimping reduces the resistance to delamination by lowering bridging tractions across incipient delamination cracks.

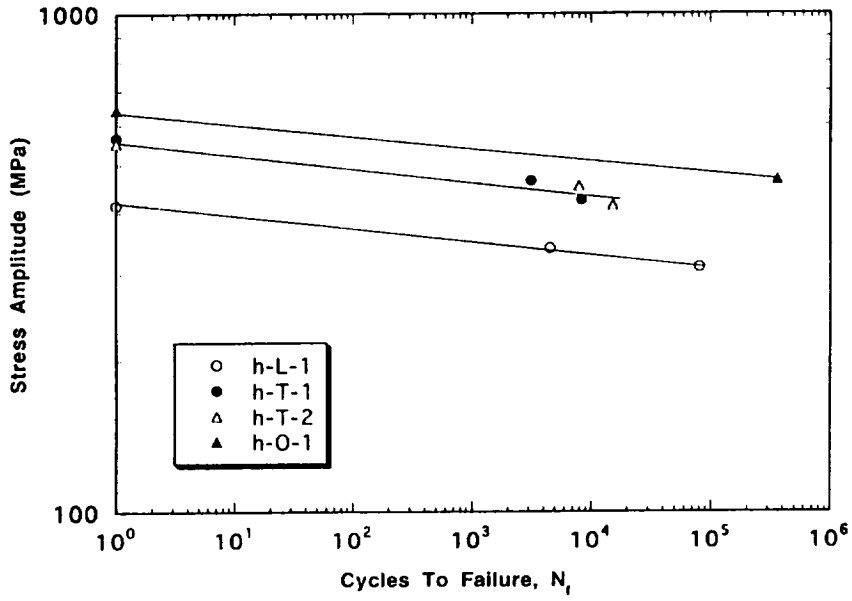

Fig. 17 Load-life data for heavily compacted composites under compression-compression loading (load ratio R = -∞).

The mechanics of failure in fatigue and monotonic compression.are evidently different. Under monotonic loading, stuffer failure was preceded by extensive debonding of both warp weavers and stuffers from the surrounding matrix, with the former debonding events apparently initiating the latter in many cases. In fatigue, the order of events was quite different. Figure 18 shows the state of damage observed on the gauge section in a micrograph that was fortuitously shot just a few cycles before failure in a specimen of type ℓ-L-1. While failed stuffers can easily be seen, all warp weavers remain well bonded to the surrounding matrix. There is indeed very little matrix cracking, in striking contrast to observations for monotonic loading. This feature has been confirmed by sectioning fatigued specimens. While sectioning revealed interior stuffer kink band

Fig. 18 One of the cut surfaces of a specimen of layer-to-layer angle interlock weave (ℓ-L-1) just prior to failure in compression-compression fatigue.

failures, the only matrix cracking appeared to be *caused by* those stuffer failures, rather than being a *cause of* stuffer failures, as in monotonic loading.

We infer that stuffer failure occurs in fatigue by the accumulation of damage *within* an individual stuffer. The damage is not triggered by events external to the stuffers, such as debonding or other matrix cracking that might allow buckling. Instead, cyclic loading slowly weakens the resin within the stuffer, reducing load transfer between neighboring fibers and therefore the critical load for kink band formation.

One fundamental characteristic pervades observations for both monotonic and cyclic loading. In both cases, woven composites exhibit damage tolerance, showing high strain to failure in monotonic loading and significantly sloping S-N curves in fatigue. Furthermore, post-mortem observations in both cases reveal damage distributed throughout the gauge section, in contrast to the case for stitched laminates, which fail by highly localized kink bands in either monotonic loading or fatigue.

4.2 Tension-Tension and Tension-Compression

The progression of damage under tension-tension or fully reversed loading is distinguished from that in compression-compression fatigue by the relatively early appearance of matrix cracks

normal to the applied load axis. These microcracks increase in density with cycles and occur at tensile amplitudes in the elastic regime of monotonic tension data.

Although the matrix cracks cause a modest increase in specimen compliance, ultimate failure is the result of tow rupture. Neither is there any evidence that the matrix cracking directly induces tow failure. Instead, it would appear that just as in compression-compression fatigue, tow rupture in tension signals the maturation of degradation that is internal to the load bearing tows. There is again correlation between sites of rupture and misalignment.

5. Models Appropriate to Different Aspects of Composite Behavior

The experiments reported above and elsewhere suggest that the mechanical properties of 3D composites can be separated into two categories: those that can be predicted to within experimental scatter by elementary models; and those than cannot, i.e., those for which our Binary Model is designed. Table 12 summarizes this classification.

Problems for Which the Binary Model is not Required

Flat panels consisting of a single weave type behave as orthotropic bodies in the elastic regime. Elastic constants are well approximated by combining rules of mixtures or other simple models of unidirectional composites with orientation averaging models (or even standard laminate theory) and some crude estimates of the softening effects of tow irregularity.

Unnotched strength in tension can be estimated from the strength quoted for pristine fibers by the manufacturer, corrected for volume fractions. Unnotched strength in compression is governed by the mechanics of kink band formation, following Eq. (4).

The extent of fiber pullout observed in unnotched tension tests (e.g., Fig. 10) suggests that notch sensitivity in tension should be modeled via a cohesive zone of damage extending from any stress concentrator. Within the cohesive zone, the mechanics of tow pullout will govern the relation p(u) between the bridging tractions, p, acting across the damage zone and the displacement discontinuity, 2u (or crack opening displacement, u). In Section 3, the characteristic cohesive zone length, l_{ch}, was shown to be to order of magnitude 0.1-0.5 m. The function p(u) can be deduced directly from measurements of force and displacement on unnotched tensile specimens, as long as the specimen width is much less than l_{ch}, e.g., ~ 10 mm. Once p(u) is known, notch sensitivity and the influence of part size and geometry on strength can be computed from the relatively simple and well developed fracture mechanics of cohesive zones or bridged cracks.

Table 12

Predicting the Properties of 3D Composites

(i) Some Properties Predicted by Simple Models

Property	Model
Stiffness of flat coupons	Rule of mixtures/mean field models Laminate theory Rough estimates of the effects of tow irregularity
Unnotched strength for aligned loads	Compression: criterion for kink band formation Tension: tow rupture strength
Notch sensitivity/fracture toughness in tension	Cohesive zone model
Delamination and buckling	Beams or plates on an elastic foundation

(ii) Some Problems Requiring a Computational Model (the Binary Model)

Problem	Remarks
Stiffness/strength of integral structures	Require stress distribution in tows in complicated arrangements
Progression of damage in monotonic loading and fatigue Localization/delocalization of damage Open-hole compression Fatigue near stress concentrators Constitutive law for cohesive zone in tension	Depend on local stress distributions, distributions of flaws, and load redistribution following local failure—stochastic problem

Delamination and subsequent buckling under monotonic compression, the primary mechanism of failure against which 3D reinforcement has been introduced into polymer composites, can also be modeled relatively simply. The delamination problem can be modeled by a variant of existing laminate theories in which elastic springs couple separable laminae (e.g., [29]). For 3D composites, the springs represent the through-thickness reinforcement. The problem of buckling of delaminated layers in 3D composites can be described as that of classical buckling plates on an elastic foundation [25,26].

For nearly all of the above properties, the 3D composite behaves essentially as a laminate of homogeneous layers. The effects of the 3D weave or of irregularity in tow positioning are either small or are determined by averages over large volumes of material. The sole exception is modeling based on the concept of a cohesive zone, for which the crucial relation p(u) depends strongly on the irregularity and geometrical details of the reinforcement. However, engineering predictions

based on the cohesive zone model can be completed by determine p(u) experimentally; for this particular purpose, the micromechanics underlying p(u) need not be modeled in detail (e.g., [30]).

Problems to be Solved by the Binary Model

Other important problems defy such relatively simple modeling. They are generally those in which macroscopic behavior depends on the details of load distribution throughout the composite. Some examples are given in part (ii) of Table 12.

One very important application of 3D composites is the fabrication of integral structures. Two examples from weaving technology are integral box beams, containing predominantly axial yarns (stuffers) in the upper and lower surfaces, with ±45° yarns (warp weavers) in the sides[1]; and integrally woven skin/stiffener panels (e.g., [31]). Because of the complex reinforcement architecture in such structures, orientation averaging models are unlikely to be reliable even in the elastic regime, especially at critical junction regions such as where two sides of a box beam or a stiffener and skin merge. Predictions of stiffness and strength require the calculation of loads in geometrically complex arrangements of tows.

While the effects of complex tow arrangements present a deterministic problem, several other aspects of composite behavior depend on how random flaws are distributed in both strength and space. These properties demand a stochastic model.

In compression, the more misaligned segments of tows will fail by kink band formation at lower values of the local axial stress, following Eq. (4). If lateral loads also act on a tow as from tow wrap-around, an additional shear stress, τ_l, is induced. For the simplest assumptions concerning local fiber and kink band geometry, σ_k is lowered further according to [15]

$$\sigma_k = [\tau_r - \tau_l] / \phi_k \qquad (12)$$

The tensile rupture of tows has not been quantitatively modeled. However, it seems plausible that segments of tows that are unusually bent, squashed, or subjected to lateral loads will have reduced tensile strength.

In both compression and tension, fluctuations in tow alignment also affect the onset of nonlinearity by causing uneven load distribution. A tow segment with unusually high waviness is

[1]Ray Edgeson, Cambridge Consultants, Cambridge, UK; private communication, 1992.

more compliant under axial loading than one that is already straight. Straighter tow segments will therefore bear a disproportionate share of the load and tend to fail early in loading.

Thus the onset of damage, whether under monotonic or cyclic loading, must depend on the distribution of flaw strengths and the evenness of load distribution. The progression of damage at higher strains will depend on both of these factors as well as the way loads are redistributed around a local failure event. In both compression and tension, load redistribution around a kinked or ruptured tow is mediated by friction acting around the periphery of the broken tow. The critical stress for frictional sliding dictates the distance along the failed tow over which the tow is reloaded to far field loads by load transfer, and it therefore dictates the range of interaction of flaws.

One important characteristic of damage progression is whether successive local failure events form a localized band of macroscopic damage or whether they are delocalized and widely distributed over the gauge section. A transition from localized to delocalized damage, manifested as a brittle-ductile transition in compressive stress-strain curves, has already been noted for 3D stitched and woven composites (Section 3). Quantitative analysis of the transition requires the binary model, with an appropriately detailed solution of the statistics of local failure events and load redistribution. Modeling the transition from localized to delocalized damage is the key to modeling strain to failure and damage tolerance.

While predictions of notch sensitivity in tension can be made using an empirically determined constitutive law, p(u), in a cohesive zone model, composite design requires understanding how p(u) is determined by microstructure. Tow pullout lengths are determined partly by the flaw distribution within tows, wider distributions favoring long pullout lengths (e.g., [18,19]. Pertinent flaws comprise both intrinsic strength variations and geometrical irregularities, especially locations where cross tows might impose weakening lateral loads on an aligned tow. Pullout loads are also influenced by transverse compression experienced by ruptured tows, since pullout is resisted by friction. Transverse compression can be strongly enhanced by through-thickness tows, which often survive the rupture of neighboring axial tows, by the mechanism illustrated in Fig. 19. Computing how all these factors of reinforcement architecture and irregularity influence p(u) is another application of the Binary Model.

The likely success of cohesive zone models for predicting notch sensitivity in tension is due to the large values estimated for the characteristic cohesive zone length, l_{ch}. Since damage is spread over such large lengths before failure, details of the tow geometry near the stress concentration have minimal effect. Stochastic quantities are sensed only in their averages over the cohesive zone.

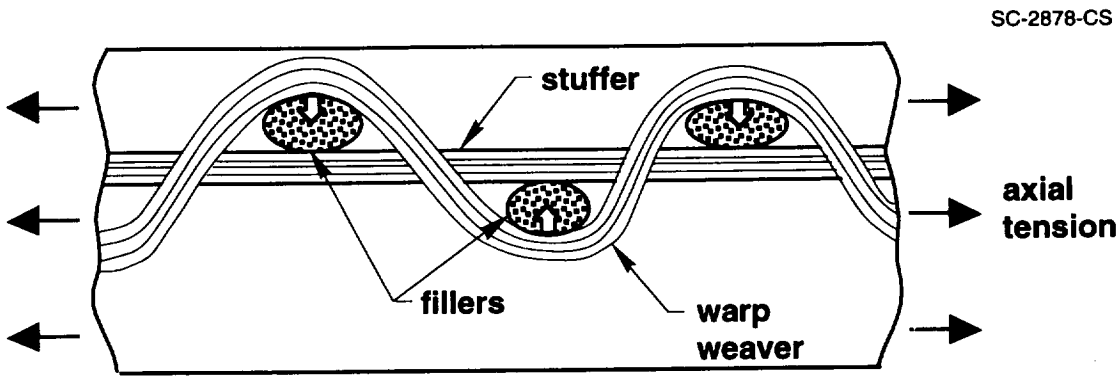

Fig. 19 Schematic of the development of transverse compression by warp weavers during tensile loading. White arrows indicate the sense of loads imposed on neighboring tows by warp weavers, which tend to straighten when strained in the direction of the load, even in the elastic regime. The case shown is a layer-to-layer angle interlock weave.

In compressive loading or cyclic loading, where tow pullout lengths may not be as large as in monotonic tension, the failure process could depend more critically on events confined to a relatively small volume near a stress concentrator—perhaps containing only a few tows. If experiments show such behavior (they are in progress), the Binary Model will be required to compute the effects of notch shape, tow positioning, and random geometrical flaws.

6. Binary Model of a 3D Composite

The Binary Model is a finite element model, in which the highly anisotropic and heterogeneous structure of a 3D composite is resolved into simple constituents: reinforcing "tows", which primarily represent the axial properties of individual tows; and an "effective medium", which represents all other properties of the tows, resin pockets, voids, etc. in an average sense. The usefulness of this division rests on the fact that the axial modulus of the reinforcing fibers, whether graphite, glass, or other material, is generally two orders of magnitude greater than the modulus of the resin. The axial modulus of the fibers dominates strength and stiffness under aligned loads, while the modulus of the resin dominates properties that depend on the effective medium, notably the shear and transverse stiffnesses and Poisson's effect. When the model is discretized, the tows are divided into two-noded line elements possessing axial rigidity only, with no prescribed shear or bending resistance. The effective medium is divided into solid elements, which, at least in the elastic regime, are defined to be homogeneous and isotropic. The effective medium elements and the tow elements are coupled by imposing constraints between certain nodes of each. The constraint will usually comprise an undamaged state, in which the nodes simply share the same coordinates, and a damaged state, allowing some relative displacement. As in the real

composite, no two reinforcing tows are coupled directly. They interact only via the effective medium. Tow and effective medium elements are commensurate with the characteristic scale of the reinforcement architecture, e.g., the distance between points at which one tow crosses two other tows successively. Relatively large sections of the composite structure can thus be modeled in a calculation with a modest number of degrees of freedom. In most cases, the volume modeled is much greater than that of the hypothetical unit cell from which a geometrically ideal model could be constructed by translation and repetition. In applications to date, the size of each model calculation has usually been determined by the gauge section of some specimen being simulated.

Both tow and effective medium elements are nonlinear, with plasticity and local failure incorporated in their assigned constitutive properties. The constitutive laws for tow and effective medium elements also embody stochastic parameters.

Figure 20 shows a typical arrangement of nodes on tow and effective medium elements in a small volume of a layer-to-layer angle interlock woven composite. In this particular architecture, stuffers and fillers lie in orthogonal layers, while warp weavers supply through-thickness reinforcement by looping above and below individual fillers in adjacent filler layers. This structure lends itself to the cuboidal effective medium elements exemplified by the shaded volume in Fig. 20.

As in any discretization of a continuous (or piece-wise continuous) body, there is some arbitrariness in the choice of element size. The choice illustrated in Fig. 20 entails the minimum density of tow nodes required to reproduce the topology of the reinforcement faithfully. A higher density of nodes could be chosen, but that would betray the spirit of finding the *simplest possible* realistic formulation. Nevertheless, as well as the assurance of computational precision in modeling tows, other physical conditions must also be met in choosing the element size. These will be discussed below.

Once the element size has been chosen, the length scale it introduces determines the way geometrical fluctuations are treated. Thus, the irregularity of a tow that undulates over wavelengths larger than the element size can be mimicked simply by displacing appropriate nodes on that tow in the initial, load-free configuration of the model. If a geometrical property fluctuates over a length less than the element size, the variation must be incorporated in the constitutive law provided for that element. Some explicit examples of this will be given below.

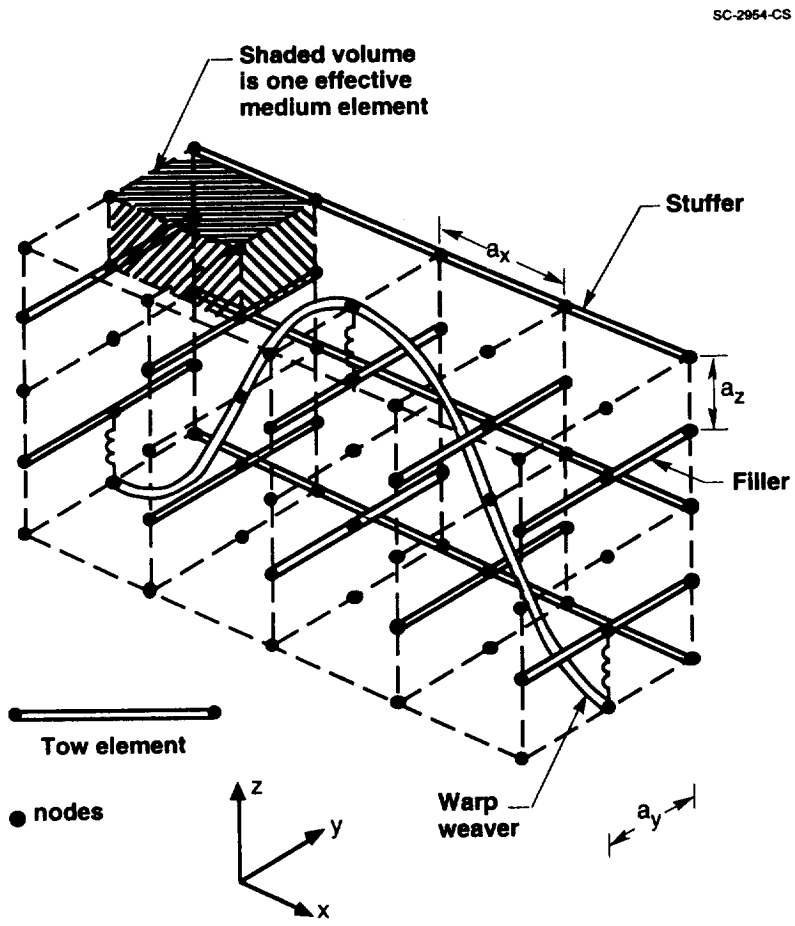

Fig. 20 Tow and matrix elements in a layer-to-layer angle interlock woven composite.

The conceptual division of the composite into tow and effective medium elements is ultimately a matter of convenience. The end product is a nonlinear finite element model, which must be equivalent to a model containing only solid elements, with the effects of the tow elements incorporated in appropriate anisotropic and nonlinear constitutive laws. However, the geometrical complexity of the reinforcement would oblige the definition of many different types of solid element in such a model, depending on the local tow configuration. Furthermore, the treatment of stress redistribution around a failed tow and the computation of local axial stresses in tows would be cumbersome.

As in any finite element model, the boundary conditions remain unspecified in the general formulation. In each application, either load or displacement conditions are specified for boundary nodes. There is no restriction in principle on the distribution of the boundary forces or displacements; or on the shape of the boundary itself.

6.1 Constitutive Laws for Tow Elements

The properties of tow elements follow from various elementary arguments.

Elastic Properties

The axial elastic modulus, E_t, of a tow that is initially straight can be estimated by the rule of mixtures:

$$E_t = V_t E_f + (1-V_t)E_r \,, \tag{13}$$

where V_t is the volume fraction of fibers within a single tow and E_f and E_r are Young's moduli for the fibers and resin, the former measured axially. The axial stiffness, k_t, of the corresponding tow element in the binary model is given by

$$k_t = (E_t - E_m)\, A_t \tag{14}$$

where A_t is the tow's cross-sectional area and E_m is Young's modulus for the effective medium (specified below). The subtraction of E_m in defining k_t avoids double counting that would arise because the effective medium elements fill all space. The area A_t is deducible from the length per unit mass, y, of the tow (known as the "yield); the density, ρ_f, of the fibers; and V_t according to

$$A_t = \frac{1}{V_t \rho_f y} \quad . \tag{15}$$

If the tow is undulating initially, its response to axial loads σ_t can be described by the differential axial displacement, u, between two points separated by some gauge length L:

$$u = L\sigma_t/E_t + L\varepsilon_u \equiv L\varepsilon \tag{16}$$

where ε_u is a strain contribution arising from straightening of the undulations. If the tow undulates over periods greater than the element size, both of these terms will be computed as part of the solution of the discretized model, with tow undulations entered explicitly as initial nodal offsets. However, if the tow undulates over periods less than the element size, the second term in Eq. (16) must be computed in advance by micromechanical modeling. The tow elements then possess a possibly strain-dependent, reduced effective axial stiffness, $E_e = d\sigma_t/d\varepsilon$.

Calculating E_e accurately is difficult. However, knockdowns due to waviness or irregularity should never lower the composite modulus by more than 10-20%: if they do, the

composite is either poorly designed or badly fabricated. Experimentally measured scatter in the macroscopic composite modulus is usually 5-10% in 3D woven or braided composites, while tow waviness itself is difficult to characterize and its statistics difficult to measure. Therefore, it is unlikely to be profitable to employ more than rough estimates for E_e. More usefully, simple models of the effects of tow waviness or irregularity allow competing composite designs to be compared or the effects of irregularity induced by processing to be estimated. Thus, E_e is simply written

$$E_e = \chi E_t \tag{17}$$

where χ is a random variable for the tow elements in a single simulation and typically $\chi \geq 0.9$.

For large strains, Eq. (17) will generally be nonlinear: an undulating tow will stiffen as it straightens. However, in most applications, it will be valid to assume that the knockdown factor χ is independent of strain. At strains high enough for tow straightening to change E_e, the composite stress-strain relation is likely to be dominated by tow and matrix failures.

In representing the resistance of the tows to lateral deflections by the stiffness of the effective medium, it is assumed that such deflections would arise from shear alone. However, at least in principle, both shear and pure bending could contribute significantly to lateral deflections. The proportions of the total deflection arising from each will depend on the length of the tow element, among other things, with long elements favoring the dominance of the pure bending contribution. A simple estimate of these effects is presented in Appendix C. *For the computational tow elements defined here and for all current applications in polymer composites, shear is the dominant mode of lateral deflection.* Thus shear stiffness is properly ascribed to the effective medium, leaving the tow elements themselves with no inherent resistance to lateral loads. This division has the added virtue of minimizing the degrees of freedom in the model.

Strength in Compression

The strength of a tow in compression is dictated by the mechanics of kink band formation, with the critical value, σ_k, of the axial stress being given by Eq. (4). Thus σ_k depends on two factors, the misalignment angle ϕ_k and the local shear stress due to lateral loads, τ_l, both of which may change as the composite responds to load. The shear stress, τ_l, in any tow element can be computed at each load increment from the shear stresses in adjoining effective medium elements.

How the misalignment angle ϕ_k is treated depends on whether the misalignment occurs over a gauge length that is larger or smaller than the tow element size. If it is larger, then ϕ_k is

computed from the nodal displacements. If smaller, then the role of ϕ_k is subsumed in the constitutive properties of the tow, which are prescribed a priori from micromechanical arguments. Misalignments can be measured from digitized photographs of specimen cross-sections: the inferred ϕ_k will generally be a random variable.

Strength in Tension

The stress σ_t in any tow element can be strongly affected by tow undulations. For undulations of wavelength greater than the element length, resulting variations in σ_t along the length of a tow are computed directly in solving the model. Undulations lying within a single element are represented by the reduced effective stiffness, E_e, of Eq. (17): thus

$$\sigma_t = E_e \varepsilon_t \,, \tag{18}$$

where ε_t is the axial strain in the tow element implied by its nodal displacements alone.

The failure of a tow in tension is modeled simply by the criterion that failure occurs when

$$\sigma_t = \sigma_t^{(c)} \,, \tag{19}$$

where σ_t is the axial stress in the tow element and the critical stress, $\sigma_t^{(c)}$, is a material property. The critical stress depends upon intrinsic flaws in the tow, including flaws associated with crimping or distortion caused by consolidation. It is a random variable whose distribution of initial values will probably always be evaluated by fitting the model to experimental data. It may be reduced during loading by lateral loads imposed on a nominally aligned tow by neighboring tows. If so, the value of $\sigma_t^{(c)}$ for elements in the aligned tow could be lowered during a simulation in proportion to such lateral loads, as measured by the maximum shear in adjacent effective medium elements.

Post-failure Properties

The most important local phenomenon following failure of a tow in either compression or tension is the transfer of load to neighboring tows. This is represented by the constitutive law coupling tow and effective medium nodes, as described in the following section. Once the tow has failed, the stiffness of the failed element is usually reduced to zero.

However, there are circumstances where experimental evidence indicates more complex behavior. One is intimated by the complex kink band structure of Fig. 21. Kink bands begin forming at strains of 1–2%, whereas ultimate failure in tests occurs at strains up to 15%, whereupon post mortem examination is undertaken. Multiple kinks, such as those in Fig. 21, have presumably developed as a succession of kinking events over such large strains. One explanation of this phenomenon is that kinks lock up after a certain amount of axial strain, whereupon the tow can again bear large loads. Further loading can lead to a new kink band, which is very likely to abut the prior damage, since that will act as a nucleation site. The mechanics of lockup and its relation to axial sliding of a failed tow are described in Appendix D. The upshot is the schematic stress-strain response for the tow element shown in Fig. 22.

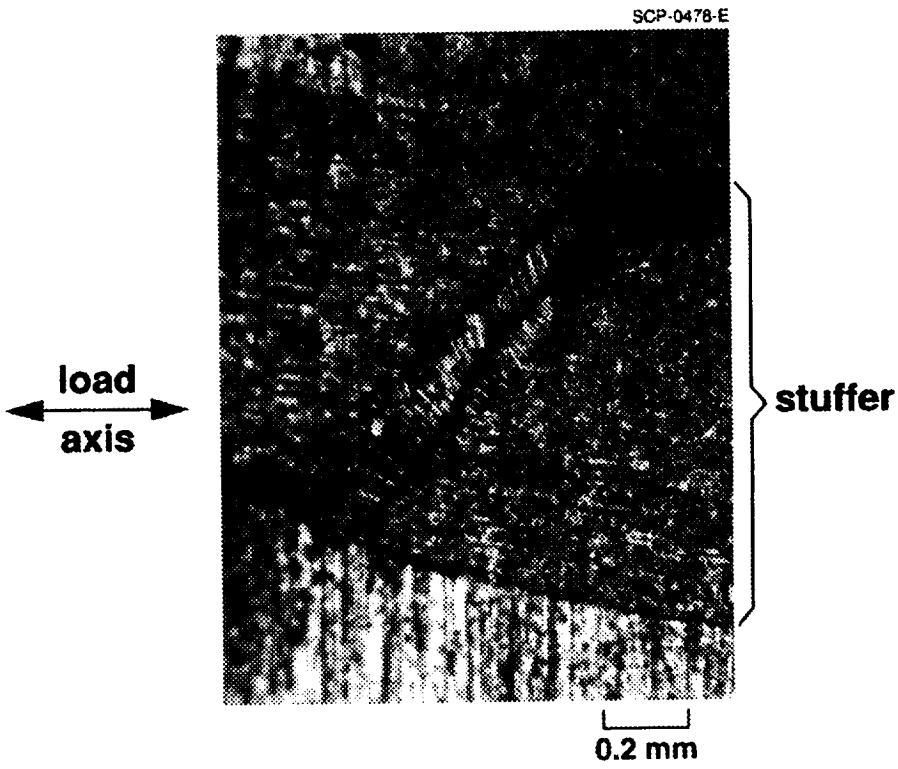

Fig. 21 System of kink bands at one site of local failure in a woven interlock composite tested to failure in uniaxial compression.

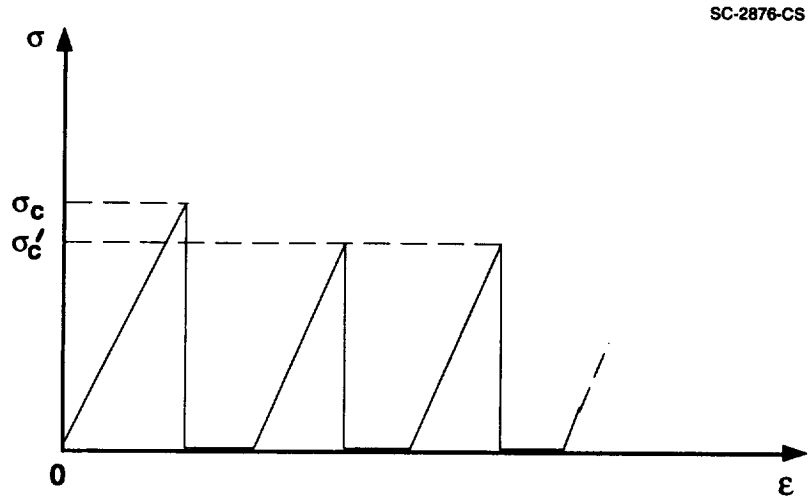

Fig. 22 Schematic of the stress-strain history of a tow element within which multiple kink banding occurs in compression.

Properties in Fatigue

The observed absence of microcracking prior to kink band formation in compression-compression fatigue (Section 4) implies that fatigue damage in compression consists of degradation of the interior of the primary load bearing tows. It has previously been pointed out [33] that fiber misalignment causes lateral or resolved shear loads in unidirectional composites that are large enough to damage the epoxy resin. In compressive fatigue loading, such damage will gradually lower the effective shear strength of the resin, which in turn will lower the critical stress for kink band failure (Eq. (4)). When that stress falls below the maximum applied compressive stress, the tow will fail. This model is consistent with the observation that kink bands form earliest in fatigue at locations of maximum misalignment. A feasible fatigue law for compressive fatigue is that

$$\frac{d\tau_o}{dN} = - A_1 (\Delta\sigma_1 \phi_k)^{n_1} \qquad (A_1 > 0)\,, \tag{20}$$

where N is the number of elapsed fatigue cycles, $\Delta\sigma_t$ the local stress amplitude in a tow element whose misalignment is ϕ_k, and A_1 and n_1 are to be evaluated empirically. The exponent n_1 could be deduced from the slope of a strain-life curve by varying the degree of misalignment achieved in processing or by comparing the cycles to kink band formation at sites that differ in misalignment.

In tensile fatigue loading, the first evident fatigue damage is matrix cracking normal to the load axis (Section 2.2). This will be dealt with below under the constitutive properties of the effective medium. Matrix damage is followed by tow rupture. The rule of mixtures demonstrates that the increase in load in the aligned tows because of matrix cracking must be slight. More importantly, tow misalignment might be expected to introduce significant shear stresses within tows in tension just as in compression, leading to direct fatigue damage of the resin within tows [33]. This might lower tow strength if fibers suffer attrition following fragmentation of the resin. A law similar to that in compression is suggested:

$$\frac{d\sigma_t^{(c)}}{dN} = - A_2 \left(\Delta\sigma_t \phi_k\right)^{n_2} \qquad (A_2 > 0)\,, \tag{21}$$

where A_2 and n_2 are further empirical parameters.

Whether Eqs. (20) and (21) are confirmed by experiments or whether tests will suggest alternative forms remains a topic of research.

6.2 Constitutive Laws for Effective Medium Elements

Elastic Properties

An assembly of tow elements such as that of Fig. 20 cannot adequately model macroscopic shear stiffness, through-thickness stiffness, or Poisson's effect. The effective medium corrects these deficiencies.

One face of a typical effective medium element is outlined on the micrograph of an angle interlock composite shown in Fig. 23. It contains resin pockets and parts of tows oriented in various directions. While its elastic properties are complex in detail, those that remain after the axial stiffness of tows has been removed to tow elements can be approximated very simply in their spatial average. For most composite properties, it is a fair approximation to assume that the effective medium is homogeneous and isotropic in the elastic regime, with properties given by rules of mixtures. Let G_f and G_r be the shear moduli and ν_f and ν_r Poisson's ratios for the fibers and resin. Then the shear modulus G_m and Poisson's ratio ν_m for the effective medium can be written

$$\frac{1}{G_m} \simeq \frac{V_f}{G_f} + \frac{1\text{-}V_f}{G_r} \tag{22a}$$

and

$$\nu_m \simeq V_f \nu_f + (1 - V_f) \nu_r \quad , \tag{22b}$$

where, making due allowance for resin pockets and fluctuations in tow density, V_f is the volume fraction of all fibers averaged over the composite, as measured, for example, by weighing the fibers after removing the resin by acid digestion.

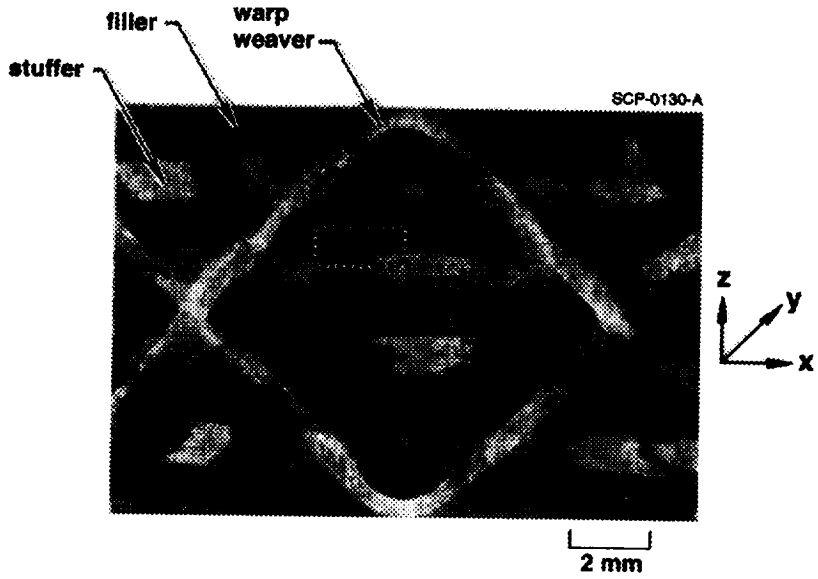

Fig. 23 A section of a through-the thickness angle interlock woven composite, consisting of AS4 carbon tows in an epoxy resin matrix. The rectangle outlines one face of a typical effective medium element.

Strength

Tensile failure of effective medium elements occurs, for example, in the delamination of layers of stuffers and fillers during compression or in the formation of matrix cracks normal to the load axis under monotonic or cyclic tensile loading. The strength of an effective medium element is denoted $\sigma_m^{(c)}$. Examination of many micrographs reveals that the most important cracks form in layers of resin between tows rather than within the tows themselves.[2] Therefore, $\sigma_m^{(c)}$ is likely to reflect the properties of the resin. However, $\sigma_m^{(c)}$ will also depend strongly on the geometrical

[2]Some microcracks are formed within tows when high through-thickness compaction loads are applied during processing. Such cracks have no effect on damage progression that has been observed as yet, although they could conceivably lower the critical stress for kink band formation and accelerate fatigue damage within tows.

details of local fluctuations in tow deployment, resin porosity, etc., which are extremely difficult to measure or model. Furthermore, the grid is so coarse that the value of $\sigma_m^{(c)}$ at which matrix crack propagation occurs for a given value of the applied load is likely to depend on the element size. Therefore, $\sigma_m^{(c)}$ will usually be treated as a model-dependent, empirical parameter.

In fatigue, one might conjecture a law paralleling Eqs. (20) and (21):

$$\frac{d\sigma_m^{(c)}}{dN} = - A_3 (\Delta\sigma_m)^{n_3} \qquad (A_3 > 0) , \tag{23}$$

where A_3 and n_3 are empirical parameters and $\Delta\sigma_m$ is the cyclic stress amplitude in the effective medium element.

For failure in either monotonic loading or fatigue, experiments show that the fracture plane almost always either separates pairs of adjacent tows or separates layers of tows. For a model geometry such as that of Fig. 20, the relevant component of stress to be compared with $\sigma_m^{(c)}$ will accordingly lie in one of the Cartesian directions shown in Fig. 20. It should be averaged over the tow element, since computed variations within an element depend on the choice of element size.

Post-failure Properties

After failure, an effective medium element will have no remanent strength in tension, but will continue to support load in compression. It can also bear tensile loads in directions orthogonal to the plane in which it failed. For example, the microcracks observed normal to the load axis in tension-tension fatigue diminish the axial stiffness but do not necessarily imply the delamination of stuffers and fillers. Thus, after failure, effective medium elements are anisotropic.

6.3 Constitutive Laws for Coupling Springs

Coupling Between Tow and Effective Medium Elements

When a tow fails, whether in axial compression or tension, stress redistribution is governed by sliding of the broken tow parallel to its axis in the vicinity of the failure site. Experimental observations suggest that sliding is Mode II displacement of a circumferential debond crack. A reasonable description of the redistribution of load is given by the shear lag model of Fig. 24(a). In the shear lag model, load is transferred from the tow to the surrounding composite (or "effective medium" in the binary model) via a constant frictional shear stress, τ_f, acting over the

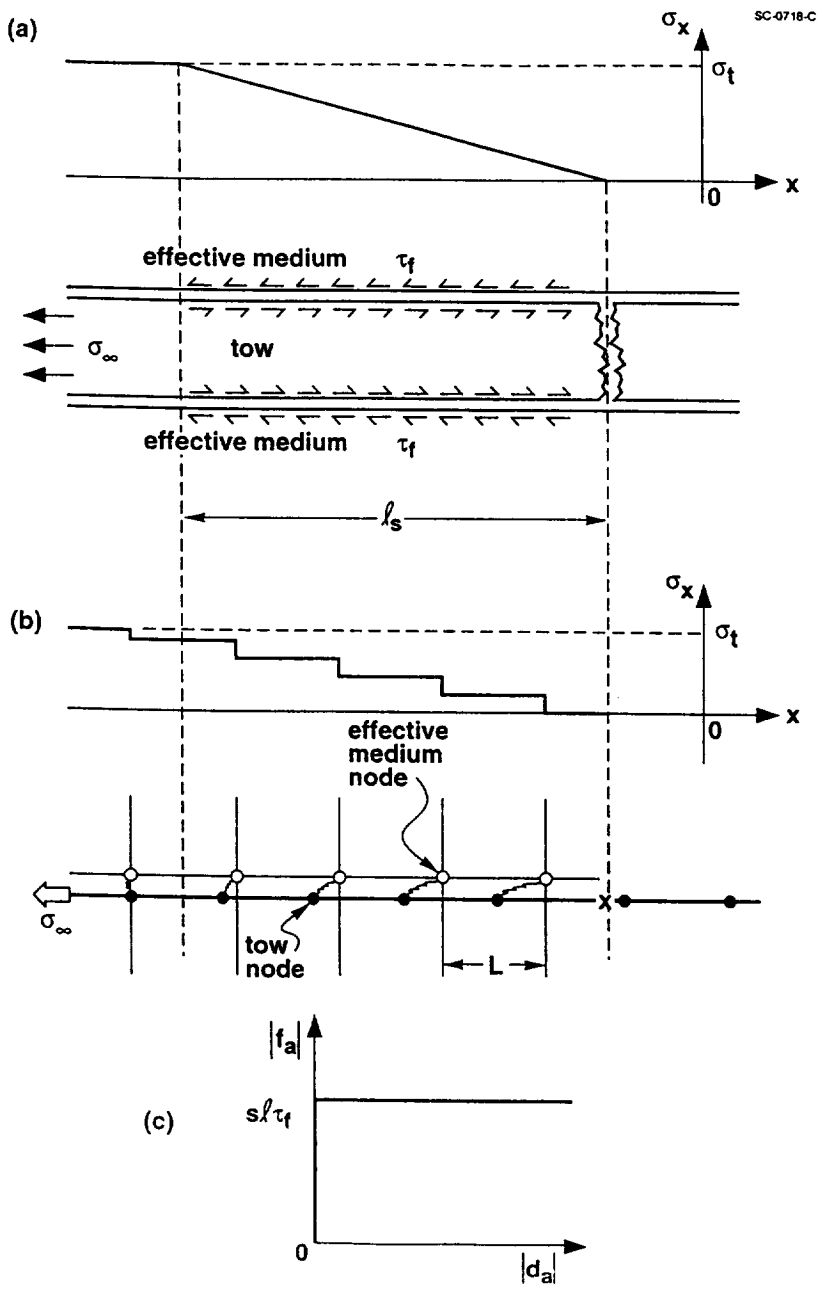

Fig. 24 (a) Shear lag depiction of stress redistribution near a site of tow failure. (b) Analog of (a) in the binary model. Tow and effective medium nodes have been drawn in (b) with different vertical coordinates solely to make them separately visible. Under axial loads, only their horizontal coordinates could differ in the orientation shown. (c) The constitutive law for axial displacements coupling springs between tow and effective medium elements.

sliding boundary. The shear tractions restore the axial load, σ_x, in the tow from zero at the site of failure to the far field[3] value, σ_t, over a characteristic length, l_s, given by force equilibrium:

$$l_s = \frac{\sigma_t}{|d\sigma_x/dx|} \tag{24a}$$

$$\left|\frac{d\sigma_x}{dx}\right| = \frac{s\tau_f}{A_t} \tag{24b}$$

where s is the circumference of the tow and A_t its cross-sectional area.

If the binary model is to describe stress redistribution correctly, then the gradient of axial stress in a tow near a failure site must have the value given by Eq. (24b), at least in its spatial average. This can be assured by appropriate specification of the constitutive laws for the nonlinear springs coupling tow and effective medium nodes. The discontinuity in the axial load in successive tow elements near the site of tow failure is simply the axial force, f_a, imposed by the coupling spring. The axial load in tow elements near the site of failure is therefore the staircase function shown schematically in Fig. 24(b). This function will have the same average gradient as $\sigma_x(x)$ in Fig. 24(a) provided

$$|f_a| = s\tau_o L \quad , \tag{25}$$

where L is the computational element length. Equation (25) prescribes a force that is independent of the relative displacement, d_a, of the relevant tow and effective medium nodes in the axial direction, as in Fig. 24(c).

The relative axial displacement of the nodes it couples is the only degree of freedom needed for a coupling spring between a tow and the effective medium. The tow and effective medium nodes always coincide in their lateral displacements.

In the common case that τ_o represents frictional sliding, its value should change with the transverse compression acting on the tow. The latter can be evaluated and continually updated by averaging the stress fields in adjacent effective medium elements during a simulation. In this way, the additional compressive loads introduced by warp weavers via the mechanism of Fig. 19 can be modeled.

---

[3]"Far field" refers here simply to the composite beyond the domain of sliding. Since the stiffness of tow elements is generally a random variable, the stresses in tow elements even in domains far removed from any stress concentrator do not share a unique value.

The use of coupling springs not only provides approximately correct stress recovery in a tow near a site of failure, but also avoids physically improper behavior which would otherwise arise from the fact that tow elements have no cross section.

Coupling Between Warp Weavers and Fillers

In practice, the optimum combination of in-plane and through-thickness properties is usually attained in a 3D woven composite if the warp weavers are of considerably lighter denier than the stuffers or fillers and accordingly of lower volume fraction [26]. This invites the simplification of coupling warp weavers by springs directly to the fillers around which they wrap, rather than via effective medium elements, thus reducing the degrees of freedom of the model. The locations of such springs are shown in Fig. 20, while constitutive laws for them are given in Appendix E. This simplified treatment of warp weavers is satisfactory at least for in-plane properties in the elastic regime. In modeling failure, the critical role of warp weavers is to impose lateral loads on fillers, which remains well represented.

7. Applications of the Binary Model

The binary scheme outlined above is potentially applicable to very diverse 2D and 3D woven and braided composites, given suitable definitions of grids and minor modifications of the constitutive laws. It is also ultimately a viable approach to modeling continuously reinforced structures, such as integrally woven or braided skin/stiffener components for airframes. Such longer term goals noted, the following examples and remarks address the subject materials of this program.

Monotonic Loading

The computer code written to solve the binary model was based on the ABAQUS finite element package.† Some illustrative simulations carried out with the ABAQUS-based code are presented here. They demonstrate some of the effects of introducing random strengths for tow elements and randomness in tow positioning.

The simulations were of uniaxial tension of through-the-thickness orthogonal interlock woven composites under displacement control. Cartoons of the model structure are shown in Fig. 25. Warp tow elements are shown there as ribbons, faces of effective medium elements as quadrilaterals, and sections of fillers as black dots. Each simulation modeled a section of material

† Hibbitt, Karlsson, and Sorensen, Inc., Pawtucket, Rhode Island.

containing ten distinct layers normal to the filler direction, which Fig. 25 shows in an exploded view. Six of the layers contain stuffers and two contain warp weavers. The ninth and tenth layers contain no warp tows; they are included to avoid tow elements (which should lie along tow axes) being present on specimen surfaces. Simulations were executed for both ideal and irregular tow positioning. Irregularity was introduced by offsetting the initial, stress-free coordinates of nodes. The offsets were chosen by Monte Carlo methods, i.e., using a pseudo-random number generator, according to an ad hoc random walk model. The magnitudes of the tow displacements were on average about 30% of the tow spacing in any direction.

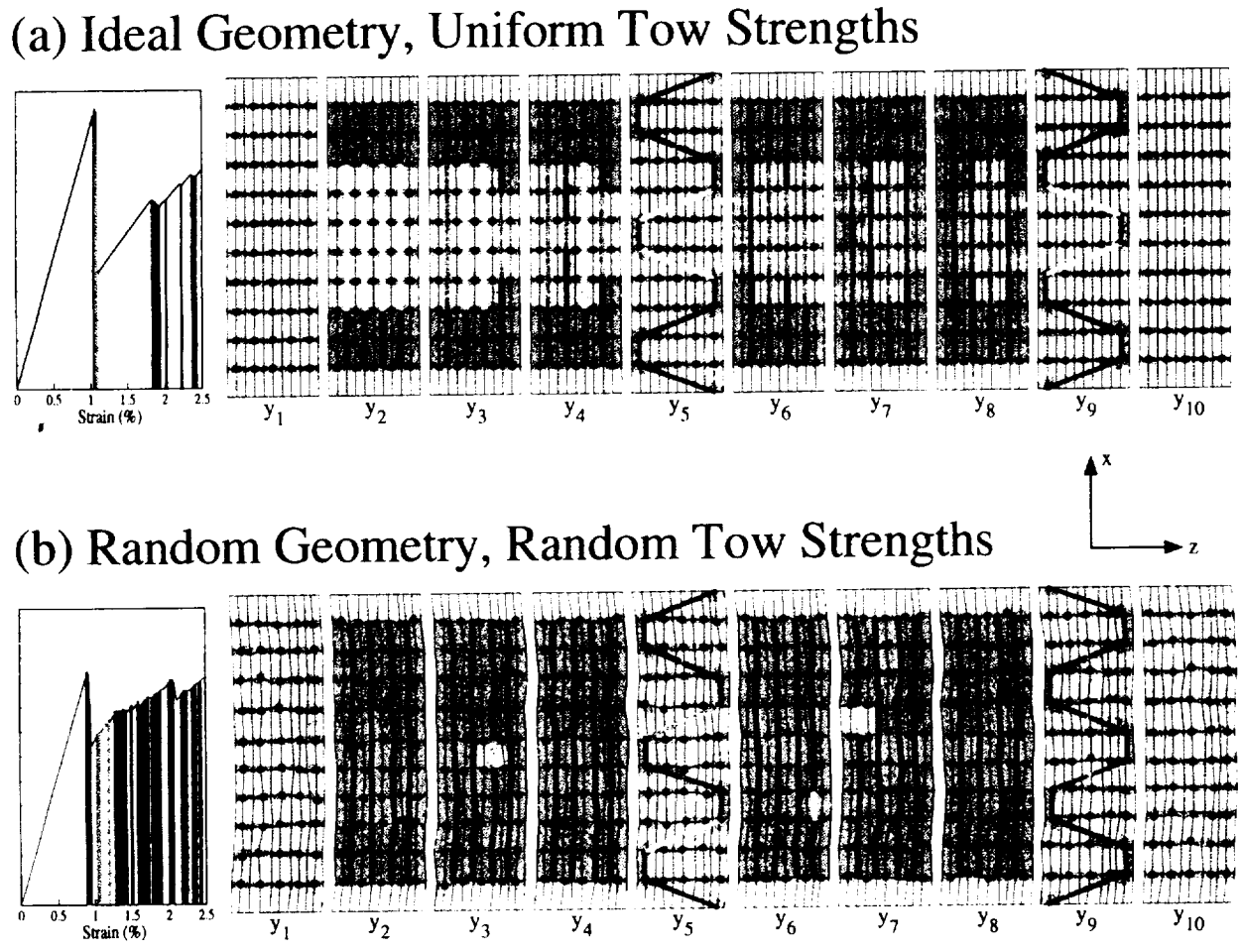

Fig. 25 Element geometry and damage sequence for orthogonal interlock composites with (a) ideal geometry and uniform tow element strengths; (b) random geometry and random tow element strengths. The inset stress strain curves contain a color code that allows the sequence of tow failures to be mapped. The ten parts in each exploded view are planes normal to the y-axis. They lie in the order indicated by the labels $y_1,\ldots,y_{10}$.

The stiffnesses of tow elements and effective medium elements, the average tow element strength, and the element dimensions that were chosen are typical of AS4 carbon tows in an epoxy resin (Table 13). The tow elements were either assigned uniform strengths (the average $\langle\sigma_c^{(t)}\rangle$ of Table 13) or normally distributed strengths with standard deviation 20% of the average. If strengths were uniform, one centrally located element was assigned a slightly lower value than the rest, to ensure that failure started away from the specimen ends. For random strengths, the lowest strength value generated was always assigned to that same element. The effective medium was assigned infinite strength: since it is so soft, the qualitative results considered here are not greatly affected.

Table 13

Specifications for the Simulations of Fig. 23

k_s (Nt)	2×10^5
k_f (Nt)	1×10^5
k_{ww} (Nt)	2.5×10^4
a_x (mm)*	2
a_y (mm)*	1.8
a_z (mm)*	0.65
E_m (GPa)	10
$\langle\sigma_t^{(c)}\rangle$ (GPa)	2
$\langle\sigma_m^{(c)}\rangle$ (GPa)	∞

* See Fig. 20 for definition

In these illustrative simulations, the degree of freedom that allows relative sliding of failed tow elements and the surrounding composite, as described in Section 6, was suppressed. (It is difficult to treat in the ABAQUS-based code.) This corresponds to the friction stress τ and therefore the stress concentration on tows neighboring a failure site both being large (but finite).

In each simulation, the applied strain was incremented in steps small enough that at most two or three and usually zero or one tow elements would fail. (Complete control is not possible in the ABAQUS-based code). The simulations were carried on to large strains.

Figure 26 shows load-strain records for uniaxial tension simulations under displacement control in the stuffer direction. The curves show the effect of successive tow failure events. Figure 26(a) is the case of ideal geometry and uniform tow element strengths. Brittle behavior is found: when one tow element fails, propagating stress concentration causes many tow elements to

fail in an unstable manner.† Only the stabilizing influence of the fixed grip loading conditions and the unrealistically infinite strength of the effective medium prevent total failure of the specimen. The other three cases (Figs. 26(b)–(d)) show the effects of irregular geometry and random strength assignments acting separately or together. Randomness in *either* geometry or strength enhances ductility.

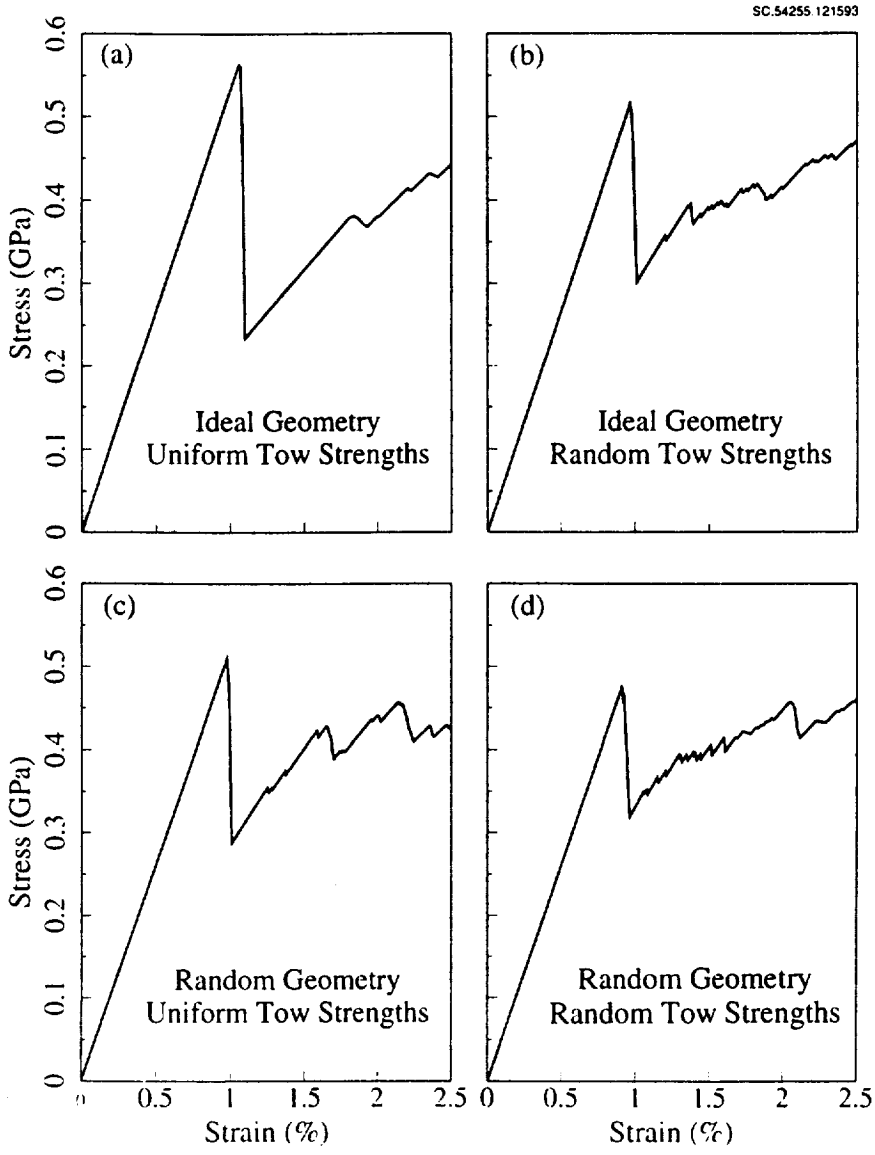

Fig. 26 Load-strain curves for various combinations of randomness of tow strength and geometry.

† In the ABAQUS-based code, all critically loaded elements must fail in a single load increment. For elements of *uniform strength*, this leads to multiple, simultaneous element failures along a single stuffer, as seen in Fig. 25(a), even when the load increment is very small. This unappealing and unphysical effect disappears as the distribution of tow element strengths broadens (Fig. 25(b)).

This trend is underscored by the failure sequence of tow elements, which has been incorporated in Fig. 25 by color coding. The value of applied strain at which any tow failed is revealed by matching its color against the color strips in the inset stress-strain record.

For ideal geometry and uniform strength (Fig. 25(a)), tow failure propagates in a symmetric, deterministic way from the first failure site. Nearly all elements on the plane on which the first failure occurred fail with very little increase in applied strain. Two elements survive, shielded by nearby warp weavers. A complete fracture path is still formed during the first load drop by the failure of the elements on either side of the two survivors. The propagating effects of stress concentration dominate the damage evolution.

In contrast, for the case of irregular geometry and random tow element strengths (Fig. 25(b)), half the tow elements on the plane of first failure remain intact throughout the entire process. Damage is distributed over the whole specimen, tending to occur in bursts in one distinct region after another. Randomness has induced a brittle/ductile transition.

The damage sequence when only one of geometry or strength is random appears intermediate between Figs. 25(a) and (b), as Fig. 26 and intuition would suggest. The patterns of failure found for random geometry or random strength are quite similar to one another. By increasing the variance of either initial node positions or tow element strengths, a brittle/ductile transition can be induced. Which one is the stronger factor in current 3D composites remains to be investigated.

Fatigue Loading

Simulations of fatigue are similar in complexity to simulations of monotonic loading, but follow different constraints. Typically, either the cyclic applied load amplitude or the cyclic applied strain amplitude is specified and held constant throughout the simulation. Damage is then measured over elapsed cycles, N, treated as a continuous variable. The strength of each element decays with N according to Eqs. (19), (20), and (22). The parameter ϕ_k is a random variable assigned an initial value for each element. The local cyclic load amplitude, $\Delta\sigma_t$ or $\Delta\sigma_m$, is computed by the model. Equations (19), (20), and (22) are integrated to identify the first element whose strength falls in fatigue to a value equal to the maximum load it bears in any load cycle. That element is then failed. The simulation is then relaxed to determined new cyclic loads on all remaining elements, which are then tested for failure without further increase in N. If none fails, Eqs. (19), (20), and (22) are integrated again, now using the new values of local stress amplitude, until another failure is found.

Ultimate failure occurs when there are sufficient failed elements to cause catastrophic damage propagation in one cycle. Quantitative examples of fatigue simulations are being conducted in our new contract.

Engineering Applications

As illustrated above, single simulations are executed by assigning random parameters (strengths and irregularity) with a pseudo-random number generator. The statistics of composite properties are then determined from an ensemble of simulations. Ultimately, calculations would be more efficient in a probabilistic formulation such as a Markov chain or diffusion equation. However, in this investigative phase, Monte Carlo methods have the great advantage that newly discovered phenomena are relatively easily programmed into the solution. In particular, the number of independent variables can be readily changed in a Monte Carlo simulation, whereas changing the dimension of a probabilistic formulation is a major programming exercise.

Input for the model consists of geometrical and material parameters, which either refer to deterministic quantities, e.g., average stiffnesses and lengths, or are parameters in the distributions of random variables. Some of the parameters can be regarded as known a priori from micromechanical arguments or measurements. Others will be empirical, having to be determined by calibrating the model against test data for the composite. A great part of current research is directed to determining which parameters fall into which category.

8. References

1. Ko, F., "Three-Dimensional Fabrics for Composites", in Textile Structural Composites, *Composite Materials, 3,* ed. T.-W. Chou and F. Ko (Elsevier, New York, 1989) Chapt. 5.

2. T.-W. Chou, R.L. McCullough, and R.B. Pipes, "Composites", *Scientific American* 254[10], 193-203, 1986.

3. J. Brandt, K. Dreschler, and R. Meistring, "The Application of Three-Dimensional Fiber Preforms for Aerospace Composite Structures", Proc. ESA Symp. on Space Applications of Advanced Structural Materials, ESTEC, Noordwijk, Netherlands, March 1990 (ESA SP-303, June, 1990) pp. 71-77.

4. M.B. Dow and D.L. Smith, "Damage Tolerant Composite Materials Produced by Stitching Carbon Fabrics", Int. SAMPE Tech. Conf. Series, Vol. 21, 1989, pp. 595-605.

5. B.N. Cox, "A View of 3D Composites", in Proc. IRC 92, Birmingham, England, September 1992, ed. M.H. Loretto and C.J. Beevers (MCE Publ., Birmingham, 1993).

6. R.E. Horton and J.E. McCarty in *Engineered Materials Handbook, Vol. 1, Composites.* (edited by C.A. Dostal), Am. Soc. Metals, Metals Park, Ohio (1987).

7. R. Palmer and F. Curzio in *Fiber-Tex 1988 Conference Proc.*, Greenville, South Carolina, 1988. NASA Conf. Publication 3038 (1989).

8. L.E. McAllister and W.L. Lachman in *Fabrication of Composites, Handbook of Composites*, Vol. 4, p. 109, Elsevier, New York (1983).

9. B.N. Cox, M.S. Dadkhah, R.V. Inman, W.L. Morris, and J. Zupon, "Mechanisms of Compressive Failure in 3D Composites", *Acta Metall. Mater.* 40, 3285-98 (1992).

10. Falcone, A., Dursch, H., Nelson, K., and Avery, W., "Resin Transfer Molding of Textile Composites", NASA Contractor Report CR 191505, July, 1993.

11. M.R. James, W.L. Morris, and B.N. Cox, "A High Accuracy Automated Strain Field Mapper", *Exptl. Mechanics* 30, 60-67 (1990).

12. M.R. James, W.L. Morris, B.N. Cox and M.S. Dadkhah, "Description and Application of Displacement Measurements Based on Digital Image Processing", in *Micromechanics: Experimental Techniques*, ed. W.N. Sharpe, Jr. (ASME, New York, 1989).

13. A.S. Argon, "Fracture of Composites", in *Treatise of Materials Science and Technology*, Vol. 1, Academic Press, New York, 1972.

14. B. Budiansky, "Remarks on Kink Formation in Axially Compressed Fiber Bundles", in *Preliminary Reports, Memoranda and Technical Notes of the Materials Research Council Summer Conference*, La Jolla, California, July 1979 (DARPA, 1979).

15. B. Budiansky and N.A. Fleck, "Compressive Failure of Fiber Composites", *J. Mech. Phys. Solids*, 41 (1993) 183-211.

16. P.T. Curtis and S.M. Bishop, "An Assessment of the Potential of Woven Carbon Fiber-Reinforced Plastics for High Performance Applications", *Composites* 15, 259-65 (1984).

17. M.R. Wisnom, "On the High Compressive Strains Achieved in Bending Tests on Unidirectional Carbon-Fiber Epoxy", *Composites Science and Technology* 43 (1992) 229-235.

18. D.M. Thouless and A.G. Evans, *Acta Metall.* 36, 517 (1988).

19. M. Sutcu, "Weibull Statistics Applied to Fiber Failure in Ceramic Composites and Work of Fracture", *Acta Metall.* 37, 651 (1989).

20. B.N. Cox and D.B. Marshall, "Concepts for Bridged Cracks in Fracture and Fatigue", *Acta Metall. Mater.*, 42 (1994) 341-63.

21. A.H. Cottrell, "Mechanics of Fracture", Tewksbury Symposium on Fracture, University of Melbourne (1963) pp. 1-27.

22. J.R. Rice, "The Mechanics of Earthquake Rupture", in *Physics of the Earth's Interior, Proceedings of the International School of Physics, "Enrico Fermi"*, ed. A.M. Dziewonski and E. Boschi (North Holland, Amsterdam, 1980) pp. 555-649.

23. A. Hillerborg, "Analysis of One Single Crack", in *Fracture Mechanics of Concrete*, ed. F.H. Wittmann (Elsevier Science, Amsterdam, 1983) pp. 233-49.

24. G. Bao and Z. Suo, "Remarks on Crack Bridging Concepts", *Appl. Mech. Review* 45 (1992) 355-66.

25. B.N. Cox, "Fundamental Concepts in the Suppression of Delamination Buckling by Stitching", in *Proc. 9th DoD/NASA/FAA Conf. on Fibrous Composites in Structural Design*, Lake Tahoe, Nevada, November, 1991, ed. J.R. Soderquist, L.M. Neri, and H. Bohon (U.S. Dept. Transportation, 1992) pp. 1105-10.

26. B.N. Cox, "Delamination and Buckling in 3D Composites", *J. Comp. Materials,* in press.

27. P.M. Jelf and N.A. Fleck, "The Failure of Composite Tubes Due to Combined Compression and Tension," *J. Mater. Sci.,* in press.

28. M.P.F. Sutcliffe and N.A. Fleck, "Effect of Geometry on Compressive Failure of Notched Composites", *Int. J. Fract.*, in press.

29. Shuart, M., "Short-Wavelength Buckling and Shear Failures for Compression-Loaded Composite Laminates", NASA TM 87640 (1985).

30. Cox, B.N. "Extrinsic Factors in the Mechanics of Bridged Cracks," *Acta Metall. Mater.* 39 (1991) 1189–1201.

31. Stover, D., "Near-net Preforms and Processes Take Shape", *Advanced Composites*, July/August 1992.

32. Slaughter, W.S., Fleck, N.A., and Budiansky, B., "Compressive Failure of Fiber Composites: The Roles of Multiaxial Loading and Creep", *J. Engng. Mater. Tech.* 115 (1993), 308-13.

33. Piggott, M.R., and Lam, P.W.K., "Fatigue Failure Processes in Aligned Carbon-Epoxy Laminates", in ASTM-STP 1110 (ASTM, Philadelphia, 1991).

Appendix A
Processing of Lightly Compacted Composites

We consolidated the lightly compacted composites ourselves, using methods developed ad hoc. The matrix in all cases was formed from Tactix 138 resin and H41 hardener.§ The preform was placed in a reusable aluminum mould, heated to 65°C, and degassed in a vacuum of ~ 1 Torr. The resin was then mixed with the hardener and also heated to 65°C and degassed. The mixture was poured over the preform (still at 65°C) and the whole assembly was degassed twice again. The first degassing typically resulted in bubbling out of some volatiles followed by apparent boiling as the pressure fell. The pressure was then cycled between 1 Torr and atmospheric pressure to remove small bubbles clinging to the mat. The mould was closed and the specimen cured, the curing cycle (chosen to maximize resin toughness) comprising 2 h at 120°C and 2 h at 177°C. All fabrication runs produced 25 x 10 cm panels, from which specimens were machined.

Figure A.1 shows representative cross sections of a through-the-thickness angle interlock specimen. There is no visible porosity in the optical micrograph of Fig. A.1(a), while the scanning electron micrograph of Fig. A.1(b) shows complete wetting of each fiber in an individual filler tow and the absence of any matrix or interfacial microcracking. If care was taken to avoid excess resin on the specimen surfaces (which was not especially easy, since the preform thickness varied), the only microcracks to be found occurred in surface pockets of resin between tows. Such microcracks would extend into the composite until they encountered the internal microstructure. Thus their average size was about the diameter of one fiber tow. The large openings of these cracks attest to the substantial, tensile residual stresses in the epoxy, which evidently drive the microcracking. However, detailed observations of failure mechanisms revealed that these initial surface microcracks have no role in compressive failure.

During impregnation and cure, a small pressure was applied through the thickness of the preform by bolting down the lid of the mould. This pressure was sufficient to ensure firm contact between the mould and the thicker parts of the preform, but not sufficient to maximize fiber packing density elsewhere.

§ Dow Chemical, Freeport, Texas.

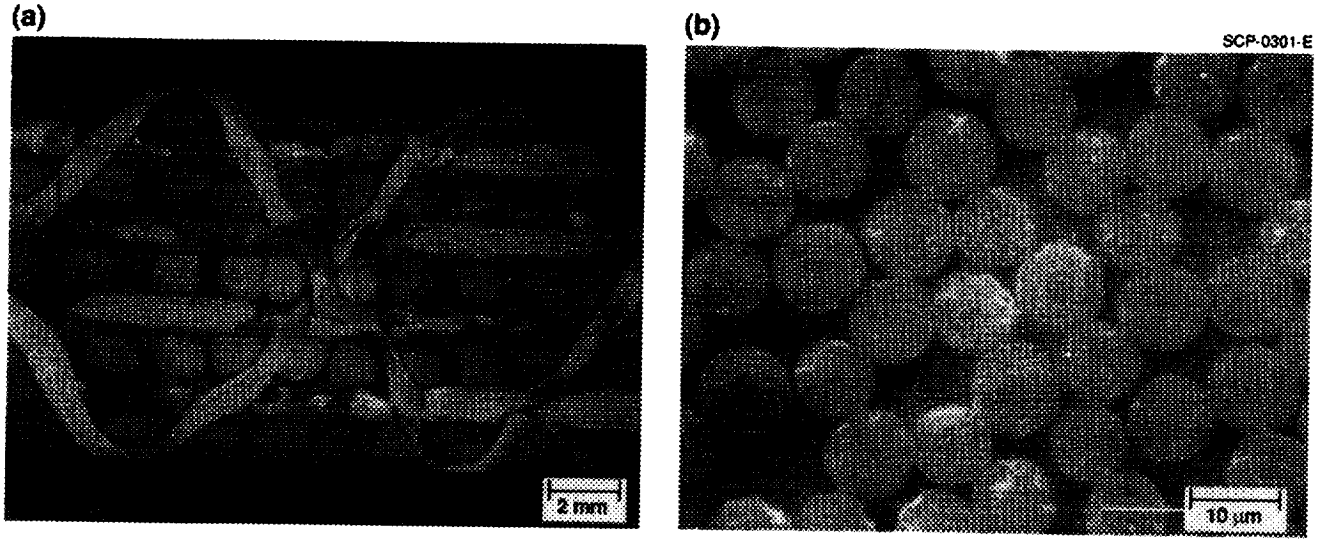

Fig. A.1 (a) Optical micrograph of section parallel to warp fibers through composite of preform *l*-T-1 of Table 1 with Tactix 138/H41 matrix. (b) SEM micrograph of section through an individual filler in (a).

Appendix B
Shear Flow Stress for Kinking of Tows

This appendix addresses the shear flow stress, τ_f, upon which the critical compressive load for kink band formation depends (Eq. (4)).

In fact, neither the Shell 1895 nor the Tactix 138 resin alone exhibits significant plastic flow except under uniaxial compression. Both appear very brittle in either tension tests or "shear" tests using Iosipescu specimens. In the latter tests, catastrophic cracking spreads from small volumes of material near the notches where tensile stresses exist. Thus properties relevant to kink band formation in composites are not observable in the neat resin. The relevant properties are those of the resin when it is under the mechanical constraint of the fibers.

One approach to measuring τ_f might be to attempt shear loading experiments on tows in the subject 3D woven composites. However, such an experiment is hard to devise and would be even harder to analyze, since the local stress state is very complicated. Tests were run instead on ±45° laminates, following work by earlier authors [27].

Laminates were available for the AS4/Shell 1895 system only. They consisted of symmetric ±45° lay-ups of "uniweave" fabric, in which AS4 and glass fibers are combined in the proportion 19:1 by volume in a plane weave. "Uniweave" is prepared to facilitate handling. The glass fibers have an insignificant effect on failure in the present context. The total volume fraction of AS4 fibers is similar in the laminates to that measured within individual tows in the 3D woven composites.

The laminates were loaded in uniaxial tension along the 0° direction. The onset of near-perfect "plasticity" in Fig. B.1 is associated with microcracks in the resin that are arrayed linearly in the fiber direction (Fig. B.2). In fact, consistent with tests on neat resin, the resin near the microcracks shows no sign of plasticity in the continuum sense. The nonlinearity in macroscopic stiffness evidently arises from the microcracks themselves or frictional sliding when an array of microcracks collapses into a band of more severe damage at high strains.

Since kink bands involve strains exceeding 1%, the pertinent domain in Fig. B.2 is that for which near-perfect plasticity prevails. The shear stress resolved in the fiber direction in any ply in the ±45° laminate is half the applied load. Thus, from Fig. B.1, $\tau_f \simeq 75$ MPa for the AS4/Shell 1895 composites.

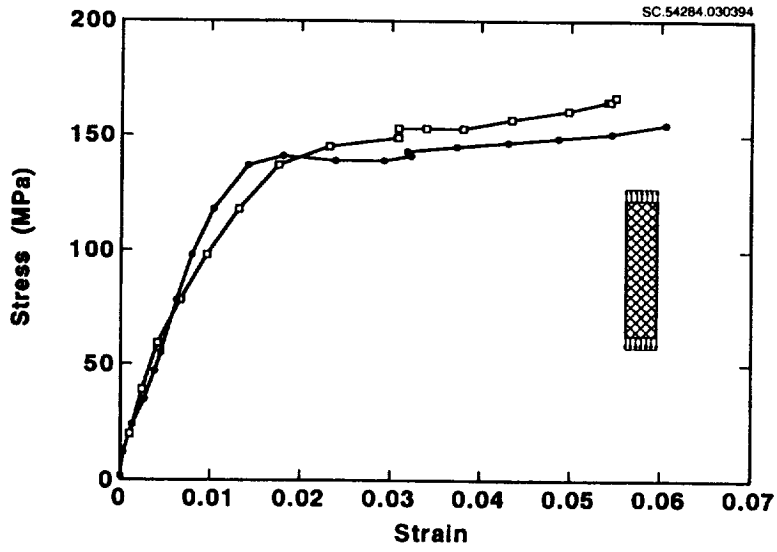

Fig. B.1 Applied load vs strain for ±45° laminates of AS4/Shell 1895 loaded in uniaxial tension along the 0° direction.

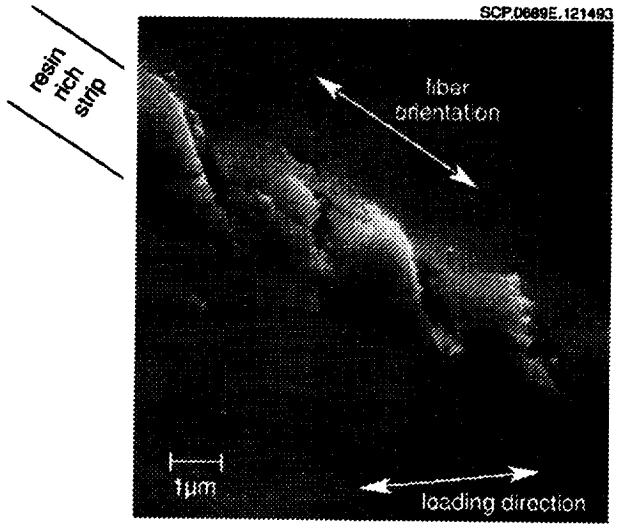

Fig. B.2 A view of the original panel surface from a tested specimen, showing a linear array of microcracks in the resin of a ±45° AS4/1895 laminate, the source of the "plasticity" in Fig. B-1. The array follows the local fiber orientation.

Similar laminates of AS4/Tactix 138 were not available for testing. However, since the Tactix 138 and Shell 1895 resins exhibit similar properties in uniaxial tension and compression, τ_f for Tactix 138 was also assigned the value 75 MPa. This must be a fair value for the rough estimates of kink band stresses in Table 7.

Appendix C
Effective Flexural Rigidity of a Tow

Consider the problem of a tow segment of length L loaded transversely by a force of magnitude F at one end (Fig. C.1). Suppose the other end is built in. The deflection $v_b(x)$ arising from bending satisfies

$$E_t I \frac{d^2 v_b}{dx^2} = Fx \,, \tag{C.1}$$

where E_t is the axial Young's modulus of the tow and I is the relevant moment of inertia; while that, $v_s(x)$, arising from shear satisfies

$$AG_t \frac{dv_s}{dx} = F \,, \tag{C.2}$$

where G_t is the shear modulus of the tow and A is its cross-sectional area. Hence the displacement contributions at the load point x = 0 are in the proportion

$$\frac{v_s(0)}{v_b(0)} = \frac{FL}{AG_t} \Big/ \frac{FL^3}{3E_t I} \tag{C.3}$$

$$= \frac{3}{4}\left(\frac{a}{L}\right)^2 \frac{E_t}{G_t} \tag{C.4}$$

for a tow of elliptical cross-section with semi-axis a in the direction of bending.

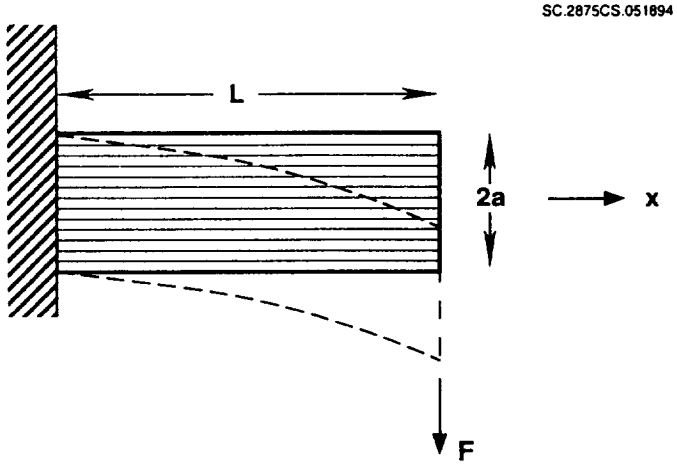

Fig. C.1 Cantilever beam paradigm for estimating the proportions of bending and shear in a transversely loaded tow segment.

The axial modulus E_t can be approximated by Eq. (13). The shear modulus G_t can be estimated by rule of mixtures from the shear moduli G_f and G_r of the fiber and resin:

$$\frac{1}{G_t} = \frac{V_t}{G_f} + \frac{1-V_t}{G_r} \quad . \tag{C.5}$$

where V_t is the volume fraction of fibers in a tow. For typical graphite/epoxy or glass/epoxy systems, the term in G_f is negligible.

The ratio E_t/G_t is typically fairly large – for AS4 graphite fibers in Shell 1895 resin, the material combination for many of the composites studied here, $V_t \simeq 0.7$, $E_f = 250$ GPa, and $E_r = 3.5$ GPa, leading to $E_t \simeq 200$ GPa, $G_t \simeq 4$ GPa, and $E_t/G_t \simeq 50$. Substituting this number into Eq. (C.4) shows that shear will dominate lateral deflections of a tow segment if a force couple acts over lengths less than five tow widths.

This criterion is satisified for forces acting on the ends of tow elements in the binary model.

Appendix D
Kink Band Lock Up

The relation between kink band lock up and the axial sliding of debonded tow segments can be elucidated by simple shear lag analysis.

Following formation of a kink band, the fiber segments within the band rotate (Fig. D.1). At first, the rotation is accompanied by transverse dilatation. But as rotation progresses, the fibers are drawn back together. At some critical rotation angle, θ_c, the volumetric strain in the band vanishes and further rotation is very strongly resisted. The band is effectively locked up. If the boundaries of the kink band form at angle β to the boundaries of the tow (Fig. D.1), the condition of vanishing volumetric strain leads to [31]

$$\theta_c = 2\beta \quad . \tag{D.1}$$

Typically, β = 20-30°.

Assume that kinking is accompanied by debonding of the tow over a sliding length l_s and that the axial compressive stress at the kink band is zero prior to lock up. Then, according to the same shear lag model that underlies Eq. (24), sliding will produce an axial displacement u of the ends of each of the intact parts of the tow given by

$$u = \frac{1}{2}\frac{\sigma_t^2 A_t}{E_t s \tau_o} \tag{D.2}$$

where σ_t is the stress in the tow remote from the kink band, A_t and s are the cross sectional area and circumference of the tow, and τ_o is the critical shear stress for sliding of the tow.

If the length of fibers within the kink band is h (Fig. D.1), lock up will occur when

$$u = \frac{h}{2}\left(1 - \cos\theta_c\right) \quad . \tag{D.3}$$

The corresponding value, σ_l, of the remote stress in the tow is

$$\sigma_l = \left[2u \bullet E_t \frac{s\tau_o}{A_t}\right]^{1/2} \quad . \tag{D.4}$$

The critical stress for lock up depends via Eq. (D.3) on the kink band length, h, which is difficult to predict.

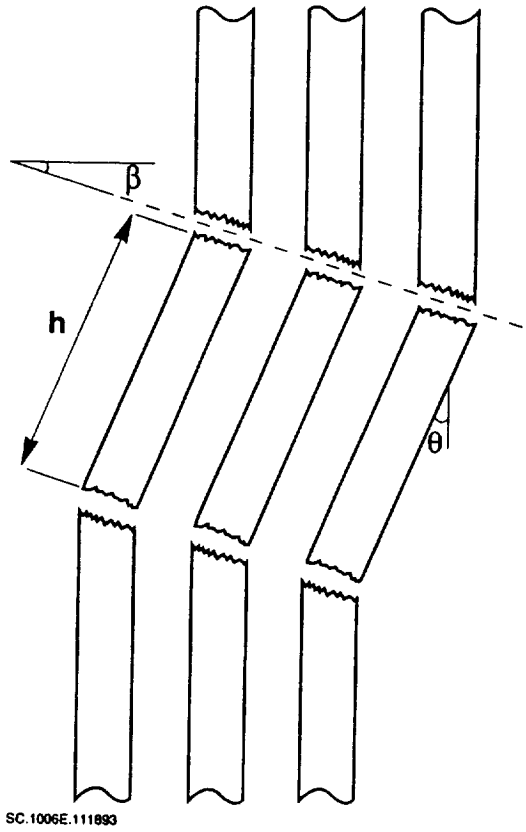

Fig. D.1 Schematic of fiber rotation within a kink band.

Appendix E
Coupling Springs Between Warp Weavers and Fillers

Figure E.1 shows a schematic of a warp weaver wrapping around a filler. The warp weaver has a radius r_w and the filler a radius r_f, which can be estimated from the fiber volume fraction, V_t, within a tow ($V_t \simeq 70\%$), the denier of the tow, and the density of the fibers. In the elastic regime, displacement of the point P on the axis of the warp weaver relative to the point R on the axis of the filler is resisted by the transverse stiffness, E_{tr}, of the two tows. This might be approximated by the rule of mixtures:

$$E_{tr} = [V_t/E_f + (1-V_t)/E_r\ ]^{-1}, \tag{E.1}$$

where E_f and E_r are the fiber and resin moduli. Assuming the contact area $4r_f r_w$ (Fig. E.1), the effective spring constant k_{wf} coupling the warp weaver and filler is defined by

$$k_{wf} = E_{tr} \cdot 4r_f r_w\ , \tag{E.2}$$

where the spring constant relates force to proportional change in displacement. Equation (E.2) can be readily generalized to the case of tows containing different kinds of fibers.

Failure of the spring occurs at some critical tensile displacement, which will usually be treated as an empirical parameter.

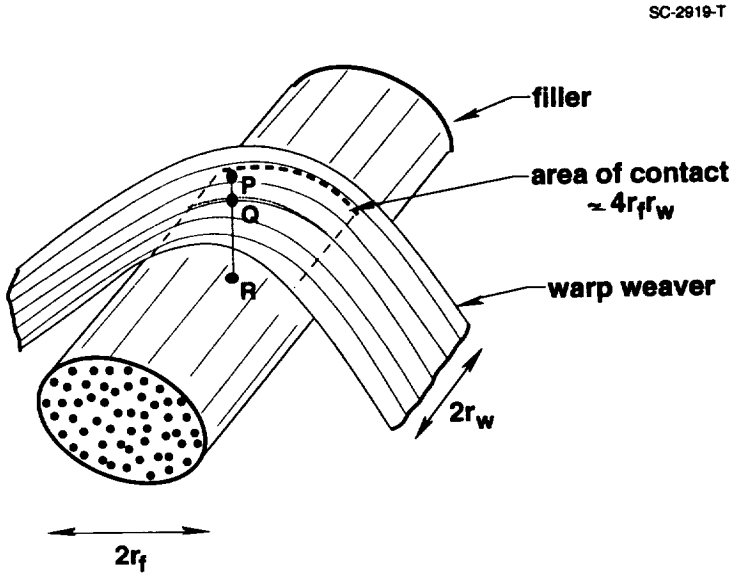

Fig. E.1 Schematic of a warp weaver wrapping around a filler in an interlock weave.

REPORT DOCUMENTATION PAGE

Form Approved
OMB No. 0704-0188

1. AGENCY USE ONLY (Leave blank)	2. REPORT DATE	3. REPORT TYPE AND DATES COVERED
	September 1994	Contractor Report

4. TITLE AND SUBTITLE

Micromechanics of Fatigue in Woven and Stitched Composites

5. FUNDING NUMBERS

C NAS1-18840

WU 510-02-12-09

6. AUTHOR(S)

B.N. Cox, W.C. Carter, M.S. Dadkhah, and W.L. Morris

7. PERFORMING ORGANIZATION NAME(S) AND ADDRESS(ES)

Rockwell International Science Center
1049 Camino Dos Rios
P.O. Box 1085
Thousand Oaks, CA 91360

8. PERFORMING ORGANIZATION REPORT NUMBER

SC71006, FRD

9. SPONSORING / MONITORING AGENCY NAME(S) AND ADDRESS(ES)

National Aeronautics and Space Administration
Langley Research Center
Hampton, VA 23681-0001

10. SPONSORING / MONITORING AGENCY REPORT NUMBER

NASA CR-4626

11. SUPPLEMENTARY NOTES

Langley Technical Monitor: C.C. Poe, Jr.
Final Report - April 21, 1989 through March 31, 1993

12a. DISTRIBUTION / AVAILABILITY STATEMENT

Unclassified - Unlimited
Subject Category 24

12b. DISTRIBUTION CODE

13. ABSTRACT *(Maximum 200 words)*

The goals of this research program were to: (i) determine how microstructural factors, especially the architecture of reinforcing fibers, control stiffness, strength, and fatigue life in 3D woven composites; (ii) identify mechanisms of failure; (iii) model composite stiffness; (iv) model notched and unnotched strength; and (v) model fatigue life.

We have examined a total of eleven different angle and orthogonal interlock woven composites. Extensive testing has revealed that these 3D woven composites possess an extraordinary combination of strength, damage tolerance, and notch insensitivity in compression and tension and in monotonic and cyclic loading. In many important regards, 3D woven composites far outstrip conventional 2D laminates or stitched laminates. Detailed microscopic analysis of damage has led to a comprehensive picture of the essential mechanisms of failure and how they are related to the reinforcement geometry. The critical characteristics of the weave architecture that promote favorable properties have been identified. Key parameters are tow size and the distributions in space and strength of geometrical flaws. The geometrical flaws should be regarded as controllable characteristics of the weave in design and manufacture.

In addressing our goals, the simplest possible models of properties were always sought, in a blend of old and new modeling concepts. Nevertheless, certain properties, especially regarding damage tolerance, ultimate failure, and the detailed effects of weave architecture, require computationally intensive stochastic modeling. We have developed a new model, the "Binary Model", to carry out such tasks in the most efficient manner and with faithful representation of crucial mechanisms.

This is the final report for contract NAS1-18840. It covers all work from April 1989 up to the conclusion of the program in January 1993.

14. SUBJECT TERMS

3D composites, interlock weaves, failure mechanisms, compression, tension, fatigue, micromechanics, failure models

15. NUMBER OF PAGES

88

16. PRICE CODE

A05

17. SECURITY CLASSIFICATION OF REPORT	18. SECURITY CLASSIFICATION OF THIS PAGE	19. SECURITY CLASSIFICATION OF ABSTRACT	20. LIMITATION OF ABSTRACT
Unclassified	Unclassified		